IRS-Assisted Physical Layer Network Coding over Two-Way Relay Fading Channels

Mahmoud AlaaEldin[*], Emad Alsusa[*], and Karim G. Seddik[†]

[*]Electrical and Electronic Engineering Department, University of Manchester, Manchester, UK M13 9PL
[†]Department of Electronics and Communications Engineering, American University in Cairo, Cairo, Egypt 11835
mahmoud.alaaeldin@manchester.ac.uk, e.alsusa@manchester.ac.uk, kseddik@aucegypt.edu

Abstract—This article investigates the performance of intelligent reflective surfaces (IRS)-aided physical layer network coding (PNC) in two-way relaying channels (TWRC). Specifically, IRS is used to eliminate carrier phase offset (CPO) at the relay node. To this end, the IRS reflectors' phase shifts are optimized to align the received signals from two source nodes at the relay. This facilitates using a simple mapping function at the relay to map the superimposed signal to a network-coded signal. Two scenarios are considered, the first of which assumes that each source node is served by a separate IRS panel, while the second scenario considers the more challenging case where only one IRS panel is available for the two source nodes. In the latter case, the IRS panel is seen by both source nodes and its phase shifts are optimized to mitigate the CPO problem while maximizing the received signal amplitude at the relay. This optimization problem is formulated and solved over the complex circle manifold. Finally, we extend the IRS-assisted PNC system to include channel coding and higher modulation orders, for which a repeat accumulate (RA) channel-coded IRS-aided PNC scheme is proposed for general quadrature amplitude modulation (QAM) signals. A belief propagation (BP) based algorithm is designed to decode the network-coded sequences over a q-Ring using modular arithmetic. Our simulation results validate the theoretical error expressions derived for the two-IRS scenario as well as the efficacy of the proposed manifold optimization approach for the one-IRS scenario. The results also confirm the efficacy of the designed channel-coded IRS-aided PNC using high QAM modulation orders.

Index Terms—Physical layer network coding, two-way relaying channels, intelligent reflective surfaces, repeat accumulate codes, sum-product algorithm, belief propagation.

I. INTRODUCTION

The application of physical layer network coding (PNC) in two-way relaying channel (TWRC) has attracted much interest by the wireless communications community during the past decade. PNC can effectively enhance the throughput of wireless networks by exploiting the broadcast nature of the wireless medium and mapping the superimposed signals at the relay during the multiple access (MA) stage to other versions of source messages, e.g., XOR or some linear combination of the original messages. In the broadcast stage, the relay forwards the network-coded signal to the source nodes so that every node can extract its intended message from the other node. PNC has been widely studied in various wireless scenarios such as non-orthogonal multiple access (NOMA) in 5G networks, random-access networks, and cognitive radio,

where it has been shown to achieve substantial throughput improvement over conventional techniques [1]–[4].

Recently, intelligent reflective surfaces (IRS) have emerged as a promising technology for wireless systems [5]–[8]. IRS is a planar surface that consists of a large number of adjustable and low-cost passive elements. These elements are able to reflect the incident signals after controlling their amplitudes and phase. The IRS technology is rising since it can be an effective solution for improving the spectral and energy efficiency of wireless networks [9]. The core characteristic of IRSs lies in their ability to customize the wireless channel from the transmitter to the receiver to achieve different design purposes like signal strengthening and interference mitigation. Therefore, and because of the aforementioned advantages, the IRS has been extensively studied in the literature during the past few years and has been applied in many application scenarios. For example, many works investigated the application of IRS in multi-user systems such as [10]–[13]. Other works have studied the application of IRS in non-orthogonal multiple access (NOMA) networks where the IRS can be optimized to maximize the sum-rate of the system whether in the uplink [14], or in the downlink [15], [16]. Other applications to the IRS were investigated in other contexts such as wireless information and power transfer [17], [18], unmanned aerial vehicles (UAV) communications [19], and physical layer security [20]. With all the aforementioned applications, the IRS has been considered as one of the vital enabling technology for the upcoming six-generation (6G) wireless networks [21].

A. Related Work

Several works in the literature were proposed to provide practical solutions to the carrier phase offset (CPO) problem between communicating nodes in PNC. The CPO problem results from the phase difference between the random fading channels between the end nodes and the relay. In several works, dealing with the PNC asynchronies, including the CPO problem, is done in the context of channel-coded PNC, where the two end nodes in the TWRC simultaneously send channel-coded packets to the relay. The relay decodes the codewords from two sources in the superimposed signals in the MA stage. The main challenge here is how the relay decodes the superimposed codewords and deduces the network-coded sequence of the raw data at both end nodes, which contains the necessary information. The authors in [22] investigated the symbol misalignment as well as CPO problems in TWRC

PNC, integrating channel coding with PNC. They proposed a general framework for jointly decoding the two packets at the relay, which can effectively deal with asynchronies while incorporating channel coding at the same time. The authors in [23] integrated irregular repeat accumulate (IRA) channel coding with TWRC PNC where both end nodes apply quadrature phase shift keying (QPSK) or pulse amplitude modulation (PAM). They proposed a linear modulation coding scheme to compute linear combinations of the data at the relay in a block fading channel by appropriately choosing the network coding coefficients in a way that best approximates the channel fading coefficients. A heterogeneous PNC scheme over a TWRC was designed and analyzed in [24], where the source nodes use different modulation orders according to their channel and traffic conditions. To overcome the CPO problem, the authors proposed an adaptive mapping function at the relay that changes based on the relative difference between the fading coefficients of both sources. The authors in [25] also proposed an adaptive PNC mapping scheme at the relay according to the channel conditions which greatly reduced the impact of MA interference. Their design was based on that every network coding map must satisfy the exclusive law by representing the maps by a 16-sides Latin square.

The authors in [26] derived lower and upper bounds on the symbol error rate (SER) of asynchronous PNC considering both phase and symbol misalignment. In [27], multiple soft-decision iterative decoding schemes for PNC, operating with coded modulation (CM) and bit-interleaved coded modulation (BICM), were proposed. The authors in [28] presented some non-linear equalization approaches for PNC systems suffering from frequency selective fading channels aiming at mitigating the distortions induced by the channel. In [29], the authors designed a joint decoding scheme at the relay for channel coded heterogeneous modulation PNC. Their decoding scheme was built on designing adaptive bit-level mapping functions which were optimized according to the two source-relay channel coefficients in the TWRC. In [30], a PNC design for network multiple-input-multiple-output (MIMO) was proposed to address the issue of high user densities in 5G networks. The proposed design criteria were set to ensure that the PNC mapping functions used at each access point overcome the singular fade states and ambiguities induced by the fading channels. The authors in [31] studied coherent detection for PNC with short packet transmissions in a TWRC operated with binary frequency shift keying (BFSK) which is less sensitive to CPO and requires less channel knowledge at the relay.

B. Motivations and Contributions

Motivated by the above works, this paper is an attempt to address the critical problem of CPO between PNC nodes by exploiting the IRS technology. As the number of reflectors in an IRS panel increases, the effect of multi-path fading diminishes because the IRS elements introduce certain phase shifts, in the form of beamforming phases to the signal rays to make them constructively add at the relay. This concept is similar to channel hardening in massive MIMO systems. To this end, we study the IRS-aided PNC system in a TWRC scenario. Firstly, we study an IRS-aided PNC scenario where two IRS panels assist the transmission, each is seen by only one end node in TWRC. Every IRS panel, in this scenario, is responsible for adjusting the fading channels of the specific node that sees it. A detailed *approximate* error performance analysis, considering the use of binary phase shift keying (BPSK) modulation at both end nodes, is provided for this scenario using the central limit theorem (CLT). The optimum detector is derived for this scenario and the corresponding approximate error probability is calculated for the IRS-adjusted fading channels at the relay.

Second, we move on to the more challenging scenario where only one IRS panel exists in the TWRC and is seen by both end nodes. In this scenario, the phase shifts of the IRS panel are optimized to jointly align the phases of the channels of both end nodes while maximizing the aggregate received signal amplitude at the relay to minimize the detection error probability. The optimization problem is formulated as a constrained maximization problem over the complex circle Riemannian manifold and then solved using an exact penalty method. Finally, we discuss the application of the presented IRS-aided PNC scenarios in practical communication systems where channel coding and high modulation orders are required[1]. We use q-ary repeat accumulate (RA)-channel-coded sequences over the ring $R = \mathbb{Z}/q\mathbb{Z}$ at both end nodes, where q is the modulation order and $\mathbb{Z}$ is the group of integer numbers. Because of aligning the two received signals from the end nodes due to the use of IRS, q can be any power of 2, which is suitable for practical communication systems. To the best of our knowledge, this work is the first attempt to deal with practical channel-coded PNC with high modulation orders in a fading TWRC. In [23], the authors presented modulation-coded PNC with high modulation orders to produce q-ary signals. However, they were forced to only use prime q values to be able to avoid ambiguity in dealing with the Rayleigh fading TWRC scenario. On the other hand, in our IRS-assisted PNC system, the IRS could cancel the channel fading effect, so we could use any practical value of q, i.e., powers of 2. A joint channel-network decoding algorithm is proposed to decode network-coded packets over the q-ring R at the relay. The decoding algorithm is based on the iterative sum-product algorithm, where we derive the necessary update rules that are required to be applied in each iteration. Simulation results are provided at the end to verify the theoretical analysis and depict the performance gains of the proposed schemes. The contributions of this work are summarized as follows:

1) A detailed approximate CLT-based mathematical analysis is performed, assuming BPSK at both end nodes, for the two-IRS aided PNC scenario, to derive an expression for the probability of XOR (of the two source nodes' data) detection error at the relay.
2) Formulate and solve an optimization problem of the phase shifts of the IRS panel in the more challenging IRS scenario where the two end nodes use the same IRS panel. The optimization problem is formulated and

---

[1]It should be noted here that the available literature on PNC in the context of TWRC has mostly focused on BPSK modulation and/or uncoded systems.
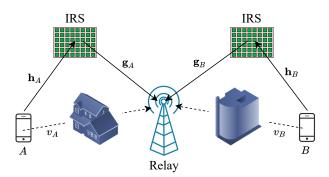
Figure 1: IRS aided PNC in TWRC (double-IRS scenario)

solved over the complex circle Riemannian manifold using manifold optimization tools.

3) Design a joint network-channel decoding scheme based on the sum-product algorithm to decode a network-coded message sequence from a superimposed RA-channel-coded q-ary sequences at the relay. The decoder exploits the IRS-adjusted received symbols at the relay to efficiently decode the superimposed codewords which are encoded over the ring $R = \mathbb{Z}/q\mathbb{Z}$.

The rest of the paper is organized as follows. In Sec. II, the IRS-aided TWRC system model is presented, while in Sec. III, the error probability of the adopted transmission scheme is analyzed. An efficient manifold-based optimization scheme is presented in Sec. IV to optimize the phase shifts of a single-IRS-assisted PNC in a TWRC scenario. In Sec. V, we discuss the design of channel-coded IRS-assisted PNC along with the associated decoding algorithm when higher order modulations at both end nodes are used. Finally, simulation results and conclusions are given in Sections VI and VII, respectively.

II. SYSTEM MODEL

In this article, we propose an IRS-assisted PNC scheme in a TWRC, where two end nodes want to exchange information using a middle relay node. The IRS-aided PNC system model adopted is shown in Fig. 1, where a separate IRS panel exists on each side of the relay to adjust the uplink channels of the corresponding end node. Every end node can see the IRS panel near to it. Every IRS panel has L reflectors where each of them introduces a different phase shift, $e^{j\theta_i}$, to the reflected signal ray. Let the two end nodes be denoted as A and B, and they want to exchange messages with the help of the relay node N_R. All the nodes are assumed to operate in half-duplex mode, i.e., the nodes cannot transmit and receive at the same time. In the TWRC, both end nodes can transmit their data to the relay node with the help of the IRS panel.

The direct node-relay channels are assumed to be independent and identically distributed (i.i.d.) Rayleigh fading channels, and they are denoted as v_A and v_B for node A and node B, respectively. The IRS-relay channel vectors are denoted as $\mathbf{g}_A$ and $\mathbf{g}_B \in \mathbb{C}^{L \times 1}$ for node A and node B respectively, and they are given as

$$\mathbf{g}_m = \sqrt{pl(d_{I_m, N_R})}\mathbf{g}_m^{Ray}, \quad m \in \{A, B\} \qquad (1)$$

where $d_{I_m, R}$ is the distance between the IRS and the relay, and $\mathbf{g}_m^{Ray}$ represents the Rayleigh fading component whose elements are i.i.d. complex normal, $\mathcal{CN}(0, 1)$, random variables.

The end node-IRS channel vectors are denoted as $\mathbf{h}_A$ and $\mathbf{h}_B \in \mathbb{C}^{L \times 1}$ for A and B respectively, and they are given as

$$\mathbf{h}_m = \sqrt{pl(d_{m, I_m})}\mathbf{h}_m^{Ray}, \quad m \in \{A, B\} \qquad (2)$$

where d_{m, I_m} is the distance between the end node and its associated IRS panel, and $\mathbf{h}_m^{Ray}$ represents the Rayleigh fading component whose elements are i.i.d. complex normal, $\mathcal{CN}(0, 1)$, random variables.

The pl factor in the channel model represents the path loss which is modeled for all the channels as

$$pl(d) = \eta_0 \left(\frac{d}{d_0}\right)^{-\alpha}, \qquad (3)$$

where η_0 is the path loss at the reference distance $d_0 = 1$ m, d represents the link distance between the transmitter and the receiver, and α is the path loss exponent. Since the IRS panel is typically set up in a position where a strong path to the relay and to the end node can exist, the path loss exponents of the IRS-relay and the node-IRS links are typically higher than the path loss exponent of the direct node-relay links. Additionally, as shown in Fig. 1, we assume that our system model is located in a harsh environment where the direct node-relay channels suffer from blockages, hence the IRS pannels are used to assist the communication. Consequently, the path loss exponent of the direct node-relay channels is assumed to be much higher than the path loss exponent of the node-IRS-relay links.

The information exchange scenario between node A and node B consists of two stages, namely the MA stage and the broadcast (BC) stage. In the MA stage, the two source nodes simultaneously transmit their data symbols to the relay node, N_R. Hence, the relay receives a superimposed signal which is a linear combination of the two source messages weighted by the corresponding channel fading coefficients. Therefore, the relay, N_R, uses a mapping function to map the received superimposed signal to a network-coded symbol which is then broadcast to the end nodes during the BC phase. For example, the mapping function can be the XOR function. Assuming the source nodes simultaneously transmit the information symbols x_A and x_B, the received signal at the relay can be given as[2]

$$y_R = (\alpha_A \mathbf{h}_A^T \Theta_A \mathbf{g}_A + v_A)\sqrt{P_A}x_A + (\alpha_B \mathbf{h}_B^T \Theta_B \mathbf{g}_B + v_B)\sqrt{P_B}x_B + n, \qquad (4)$$

where n denotes the additive noise which is modeled as complex Gaussian with zero mean and variance σ_n^2 and Θ is a diagonal matrix whose diagonal elements are the IRS reflecting elements, i.e. $\Theta = \text{diag}\{e^{j\theta_{m,1}}, e^{j\theta_{m,2}}, \ldots, e^{j\theta_{m,L}}\}, m \in \{A, B\}$, with $\theta_{m,i} \in [0, 2\pi]$ representing the phase shift introduced by the i-th IRS reflecting element. The values P_A and P_B represents the transmit powers of node A and node B respectively. The two end nodes adjust their transmit powers according to the overall node-IRS-relay channel gain.

---

[2]In our model, we assume perfect synchronization between the two transmitting nodes, so that there is no symbol misalignment between x_A and x_B [23]–[25], [28]–[30]. Some papers have focused on the asynchronous PNC case; the interested reader is referred to [22], [32].

3

The higher the node's distance from the relay, the higher the transmit power that the node consumes to equalize the average received power of the two received signals. We will discuss how P_A and P_B are adjusted to account for the different path loss values seen by the two end nodes in the next section. The IRS angles, θ_{Ai} and θ_{Bi}, are adjusted to cancel the overall phase of the i-th path of the different copies of x_A and x_B, respectively, so that they arrive at the relay node having the same phase, i.e., aligned. This is how the IRS panels can solve the critical CPO problem between the two end nodes [22], [33] in PNC TWRC systems. Therefore, the introduced phase shift of the i-th reflector should be adjusted as $\theta_{mi} = -\theta_{h_{mi}} - \theta_{g_{mi}}$, $m \in \{A, B\}$ $\forall i$. The relay can calculate all the IRS phase shifts since we assume it has knowledge of the IRS channel fading coefficients. [3] Then, the received signal at the relay node can be written as

$$y_R = \left(\alpha_A \sum_{i=1}^{L} |h_{Ai}||g_{Ai}| + v_A\right)\sqrt{P_A}x_A$$
$$+ \left(\alpha_B \sum_{i=1}^{L} |h_{Bi}||g_{Bi}| + v_B\right)\sqrt{P_B}x_B + n. \quad (5)$$

The parameters α_A and α_B are attenuation factors at the IRS panels which are adjusted to guarantee that the two received signals at the relay have equal amplitude levels for efficient PNC detection. In the next section, we discuss how these factors are calculated. It must be noted that the attenuation factor at the IRS panel is constant per all its reflectors and is always less than or equal to one, i.e. $\alpha_m \leq 1$, which guarantees that the used IRS panels are passive. This type of IRS panels is called ϵ-relaxed passive IRS whose elements are capable of scaling the reflected signal by the same factor, between $1 - \epsilon$ and 1, for all reflector elements [37]. In the following section, we discuss the XOR-PNC mapping and detection in details when BPSK modulation is used, then an *approximate* error probability of the IRS-aided PNC system is derived.

III. ERROR PROBABILITY ANALYSIS OF THE IRS-PNC

In the previous section, we presented the IRS-aided PNC scheme in a TWRC and how the IRS panels can be used to mitigate the CPO problem caused by the wireless channel fading coefficients. In this section, the probability of error performance of the IRS-aided PNC scheme is studied, where integral forms are derived to approximate the error performance of the scheme. We assume in our analysis that both end nodes, A and B, transmit BPSK modulation symbols, i.e., x_A and x_B in (5) are carved from the set $\{1, -1\}$. In the following, we are going to derive the optimal detector and the corresponding probability of error for the XOR mapping of x_A and x_B, denoted as d_{xor}, at the relay node, conditioned on the fading channel gains. Then the derived error probability will be averaged over the distribution of the channels.

[3]This is widely accepted in the context of IRS-assisted communication [5]-[20]. This assumption is valid since some works in the literature studied the channel estimation/acquisition problem for the IRS assisted systems [34]–[36].

A. Optimal detector

In this subsection, we derive the optimal decision rule assuming that no attenuation is done at the IRS panels to equalize the amplitudes of the two received superimposed signals, i.e., α_A and α_B in (5) are set to 1. Since we are only interested in detecting the XOR mapping of x_A and x_B in (5), then the optimal decision rule should only detect whether x_A and x_B have same values ($d_{\text{xor}} = 0$), or they are different ($d_{\text{xor}} = 1$). Hence, the optimal decision rule is given as

$$\Pr(x_A = 1, x_B = 1|y_R) + \Pr(x_A = -1, x_B = -1|y_R) \underset{d_{\text{xor}}=1}{\overset{d_{\text{xor}}=0}{\gtrless}}$$
$$\Pr(x_A = 1, x_B = -1|y_R) + \Pr(x_A = -1, x_B = 1|y_R). \quad (6)$$

Assuming that $\gamma_A = \sum_{i=1}^{L} |h_{Ai}||g_{Ai}| + v_A$ and $\gamma_B = \sum_{i=1}^{L} |h_{Bi}||g_{Bi}| + v_B$ in (5), then the received signal at the relay can be expressed as

$$y_R = \sqrt{P_A}\gamma_A x_A + \sqrt{P_B}\gamma_B x_B + n. \quad (7)$$

Hence, the optimal decision rule in (6) can be reduced to

$$\exp\left\{\frac{-|y_R - \sqrt{P_A}\gamma_A - \sqrt{P_B}\gamma_B|^2}{2\sigma_n^2}\right\} + \exp\left\{\frac{-|y_R + \sqrt{P_A}\gamma_A + \sqrt{P_B}\gamma_B|^2}{2\sigma_n^2}\right\} \underset{d_{\text{xor}}=1}{\overset{d_{\text{xor}}=0}{\gtrless}}$$
$$\exp\left\{\frac{-|y_R - \sqrt{P_A}\gamma_A + \sqrt{P_B}\gamma_B|^2}{2\sigma_n^2}\right\} + \exp\left\{\frac{-|y_R + \sqrt{P_A}\gamma_A - \sqrt{P_B}\gamma_B|^2}{2\sigma_n^2}\right\}. \quad (8)$$

As we can see in (8), the decision rule of the optimal detector is computationally complex as no simple thresholds can be calculated to ease the detection process. Therefore, in the next sub-section, we present an efficient sub-optimal detector whose detection rule is based on simple thresholds. Then, we will calculate the error probability that corresponds to the presented sub-optimal simple detector.

B. Sub-optimal detector with error probability calculations

In this subsection, we provide a simple sub-optimal detector to detect the XOR mapping from the received superimposed PNC signal at the relay. In our IRS-assisted PNC system model, there are L reflected rays from the IRS reflectors coherently added at the relay node. This constructive interference makes the reflected signal much stronger than the signal coming from the direct link as L increases. Therefore, the out-of-phase components of the two direct links, i.e. $\text{Im}(v_A)$ and $\text{Im}(v_B)$, can be neglected to simplify the detection process. Hence, the overall effective channels of the two transmitted signals seen by the relay can be approximated as

$$\gamma_A^R = \sum_{i=1}^{L} |h_{Ai}||g_{Ai}| + \text{Re}(v_A), \quad \gamma_B^R = \sum_{i=1}^{L} |h_{Bi}||g_{Bi}| + \text{Re}(v_B), \quad (9)$$

where γ_A^R and γ_B^R are the real components of γ_A and γ_B, respectively. The attenuation factors at the relay are adjusted to equalize the amplitudes of the two received signals at the relay. Specifically, if $\sqrt{P_A}\gamma_A^R < \sqrt{P_B}\gamma_B^R$, then α_A is set to 1, i.e. no attenuation, while $\alpha_B < 1$ is chosen such that $\sqrt{P_A}\gamma_A^R = \sqrt{P_B}\left(\alpha_B \sum_{i=1}^{L} |h_{Bi}||g_{Bi}| + \text{Re}(v_B)\right)$, and vice versa.

As long as the attenuation factors, α_A and α_B, in (5) equalize the amplitudes of the two received signals at the relay

from the two end nodes, then the received superimposed signal at N_R can be expressed as

$$y_R = \Gamma x_A + \Gamma x_B + n, \tag{10}$$

where $\Gamma = \min\{\sqrt{P_A}\gamma_A^R, \sqrt{P_B}\gamma_B^R\}$.

The proposed attenuation factors at the IRS panels, α_A and α_B, may result in large power loss in unbalanced channels. Specifically, if one of the two nodes (and its associated IRS) is farther away from the relay than the other node, its channel gain is expected to be much lower than that of the nearer node. Consequently, the IRS of the nearer node must apply a very small attenuation factor to align its signal with the far node, which may lead to high power loss. To avoid this problem, the two nodes adjust their transmit powers, P_A and P_B, according to their average overall channel gains seen by the relay. The expected value of the received amplitudes of x_A and x_B should be equalized by adjusting P_A and P_A so that $\mathbb{E}(\sqrt{P_A}\gamma_A^R) = \mathbb{E}(\sqrt{P_B}\gamma_B^R)$. Since $\mathrm{Re}(v_A)$ and $\mathrm{Re}(v_B)$ are Gaussian random variables with zero mean, then P_A and P_B can be adjusted as

$$\sqrt{P_A}\mathbb{E}(\sum_{i=1}^{L}|h_{Ai}||g_{Ai}|) = \sqrt{P_B}\mathbb{E}(\sum_{i=1}^{L}|h_{Bi}||g_{Bi}|). \tag{11}$$

By substituting g_{mi} and h_{mi} as in (1) and (2), the transmit powers can be related as

$$\sqrt{P_A}\sqrt{pl(d_{A,I_A})}\sqrt{pl(d_{I_A,N_R})}\mathbb{E}(\sum_{i=1}^{L}|h_{Ai}^{Ray}||g_{Ai}^{Ray}|) =$$
$$\sqrt{P_B}\sqrt{pl(d_{B,I_B})}\sqrt{pl(d_{I_B,N_R})}\mathbb{E}(\sum_{i=1}^{L}|h_{Bi}^{Ray}||g_{Bi}^{Ray}|). \tag{12}$$

Since h_{mi}^{Ray} and g_{mi}^{Ray} are all i.i.d. complex normal random variables having zero mean and unit variance, $\mathcal{CN}(0,1)$, then the two expectations in (12) must have equal values and hence the transmit powers can be simply related as

$$P_A pl(d_{A,I_A}) pl(d_{I_A,N_R}) = P_B pl(d_{B,I_B}) pl(d_{I_B,N_R}). \tag{13}$$

As long as the IRS panels align and equalize the two signals sent from the end nodes at the relay as in (10), the relay only receives one of the three values, $\{-2\Gamma, 0, 2\Gamma\}$, which refer to the XOR signal of interest. The relay, N_R, is concerned about detecting a network-coded mapping function of the two received superimposed signals, i.e., the XOR of x_A and x_B, d_{xor}. If the received value at the relay is detected as 0, then the relay decides that the two signals, x_A and x_B, are different as they cancel each other out, i.e., the XOR mapping is 1. On the other hand, if the received value at the relay is detected as -2Γ or 2Γ, then the relay decides that the two signals are the same, i.e., the XOR mapping is 0. Therefore, the optimal detector can be given as

$$\exp\left\{\frac{-(y_R-2\Gamma)^2}{2\sigma_n^2}\right\} + \exp\left\{\frac{-(y_R+2\Gamma)^2}{2\sigma_n^2}\right\} \underset{d_{\mathrm{xor}}=1}{\overset{d_{\mathrm{xor}}=0}{\gtrless}} 2\exp\left\{-\frac{y_R^2}{2\sigma_n^2}\right\}. \tag{14}$$

By expanding (14) and dividing both sides by $\exp\{\frac{-y_R^2-4\Gamma^2}{2\sigma_n^2}\}$, the detector in (14) can be further simplified to

$$\exp\left\{\frac{2\Gamma y_R}{\sigma_n^2}\right\} + \exp\left\{\frac{-2\Gamma y_R}{\sigma_n^2}\right\} \underset{d_{\mathrm{xor}}=1}{\overset{d_{\mathrm{xor}}=0}{\gtrless}} 2\exp\left\{\frac{2\Gamma^2}{\sigma_n^2}\right\}. \tag{15}$$

By substituting $\exp\{\frac{2\Gamma y_R}{\sigma_n^2}\}$ with z and after some manipulations, the detector equation can be shown to be given as

$$z^2 - 2\exp\left\{\frac{2\Gamma^2}{\sigma_n^2}\right\} z + 1 \underset{d_{\mathrm{xor}}=1}{\overset{d_{\mathrm{xor}}=0}{\gtrless}} 0. \tag{16}$$

Therefore, by solving the above second order polynomial equation and mapping z to y_R again, the thresholds of the above detection rule can be shown to be given as

$$\lambda_{1,2} = \pm\Gamma \pm \frac{\sigma_n^2}{2\Gamma} \ln\left[1 + \sqrt{1 - e^{-4\Gamma^2/\sigma_n^2}}\right], \tag{17}$$

and the corresponding detection rule is given as

$$d_{\mathrm{xor}} = \begin{cases} 1 & \lambda_2 \leq y_R \leq \lambda_1 \\ 0 & \text{otherwise.} \end{cases} \tag{18}$$

Consequently, the probability of error of the optimal detector derived above can be calculated as

$$P_e = \frac{1}{2}\frac{1}{\sqrt{2\pi\sigma_n^2}}\left(\int_{-\infty}^{\lambda_2} e^{\frac{-y_R^2}{2\sigma_n^2}}\,dy_R + \int_{\lambda_1}^{\infty} e^{\frac{-y_R^2}{2\sigma_n^2}}\,dy_R\right)$$
$$+ \frac{1}{4}\frac{1}{\sqrt{2\pi\sigma_n^2}}\int_{\lambda_2}^{\lambda_1} e^{-\frac{(y_R+2\Gamma)^2}{2\sigma_n^2}} + e^{-\frac{(y_R-2\Gamma)^2}{2\sigma_n^2}}\,dy_R, \tag{19}$$

and due to the symmetry of the bell curve and having $\lambda_1 = -\lambda_2$, then the probability of error can be further simplified as

$$P_e = \frac{1}{\sqrt{2\pi\sigma_n^2}}\int_{-\infty}^{\lambda_2} e^{\frac{-y_R^2}{2\sigma_n^2}}\,dy_R + \frac{1}{2}\frac{1}{\sqrt{2\pi\sigma_n^2}}\int_{\lambda_2}^{\lambda_1} e^{-\frac{(y_R+2\Gamma)^2}{2\sigma_n^2}}\,dy_R$$
$$= \frac{1}{2}\left[\mathrm{erf}\left(\frac{\lambda_2}{\sqrt{2}\sigma_n}\right) + 1\right] + \frac{1}{4}\left[\mathrm{erf}\left(\frac{2\Gamma+\lambda_1}{\sqrt{2}\sigma_n}\right) - \mathrm{erf}\left(\frac{2\Gamma+\lambda_2}{\sqrt{2}\sigma_n}\right)\right]. \tag{20}$$

C. Averaging Error Probability over the distribution of Γ

In this subsection, the distribution of Γ is derived then used to calculate the average probability of error of the IRS-assisted PNC system. The distribution of Γ, f_Γ, is the minimum of two independent random variables, $\min(\sqrt{P_A}\gamma_A^R, \sqrt{P_B}\gamma_B^R)$, where γ_A^R and γ_B^R are defined in (9). Therefore, the distributions of γ_A^R and γ_B^R, are first approximated using CLT, then they are used to derive the distribution of $\Gamma = \min(\sqrt{P_A}\gamma_A^R, \sqrt{P_B}\gamma_B^R)$. We calculate the distribution of γ_A^R first, then the distribution of γ_B^R is calculated similarly.

As in (9), γ_A^R has two terms. The first term, let's call it S_1, is the summation of L i.i.d. random variables, each is the multiplication of two i.i.d. Rayleigh random variables, i.e., $|h_{Ai}||g_{Ai}|$, hence the CLT can be used to derive an approximation of S_1 distribution, f_{S_1}, as $L \to \infty$. Consequently, f_{S_1} is approximated to follow a Gaussian distribution whose mean value and variance need to be calculated. Assuming that $U = |h_{Ai}||g_{Ai}|$, the expected value of U can be given as [38]

$$\mu_U = \mathbb{E}(|h_{Ai}||g_{Ai}|) = \mathbb{E}(|h_{Ai}|)\mathbb{E}(|g_{Ai}|)$$
$$= \sqrt{pl(d_{A,I_A})pl(d_{I_A,N_R})}\mathbb{E}(|h_{Ai}^{Ray}|)\mathbb{E}(|g_{Ai}^{Ray}|)$$
$$= \sqrt{pl(d_{A,I_A})pl(d_{I_A,N_R})}\frac{\pi}{2}\sigma_{Ray}^2, \tag{21}$$

where $\sigma_{Ray} = 1/\sqrt{2}$ is the standard deviation of the real or imaginary part of the complex Gaussian distribution of the

Rayleigh fading coefficients h_{mi}^{Ray} and g_{mi}^{Ray}. Let $U = XY$, then the variance of U can be calculated as

$$
\begin{aligned}
Var(U) = Var(XY) &= \mathbb{E}(X^2)\mathbb{E}(Y^2) - \mu_X^2\mu_Y^2 \\
&= [Var(X) + \mu_X^2][Var(Y) + \mu_Y^2] - \mu_X^2\mu_Y^2 \\
&= Var(X)Var(Y) + \mu_X^2 Var(Y) + \mu_Y^2 Var(X),
\end{aligned}
\tag{22}
$$

where X and Y are i.i.d. and Rayleigh distributed random variables, with μ_X and μ_Y their mean values, respectively. By substituting in (22) with the mean and variance of the Rayleigh distribution in [38], the variance of U can then given by

$$
Var(U) = pl(d_{A,I_A})pl(d_{I_A,N_R}) \frac{16 - \pi^2}{4}\sigma_{Ray}^4. \tag{23}
$$

Therefore, the mean and variance of S_1 can be given as

$$
\mu_{S_1} = L\mu_U = L\sqrt{pl(d_{A,I_A})pl(d_{I_A,N_R})}\frac{\pi}{2}\sigma_{Ray}^2 \tag{24}
$$

$$
Var(S_1) = L\,Var(U) = Lpl(d_{A,I_A})pl(d_{I_A,N_R})\frac{16-\pi^2}{4}\sigma_{Ray}^4. \tag{25}
$$

The second term of γ_A^R, $\mathrm{Re}(v_A)$, is already a Gaussian random variable whose mean and variance are given as

$$
\mathbb{E}(\mathrm{Re}(v_A)) = 0, \quad Var(\mathrm{Re}(v_A)) = pl(d_{A,N_R})\sigma_{Ray}^2. \tag{26}
$$

Finally, $\sqrt{P_A}\gamma_A^R$ is approximated to follow a Gaussian distribution since it is the sum of S_1 and $\mathrm{Re}(v_A)$, and scaled by a constant, $\sqrt{P_A}$. Then, the mean and variance of $\sqrt{P_A}\gamma_A^R$ are given as

$$
\mu_1 = L\sqrt{P_A pl(d_{A,I_A})pl(d_{I_A,N_R})}\frac{\pi}{2}\sigma_{Ray}^2
$$

$$
\sigma_1^2 = P_A\left(Lpl(d_{A,I_A})pl(d_{I_A,N_R})\frac{16-\pi^2}{4}\sigma_{Ray}^4 + pl(d_{A,N_R})\sigma_{Ray}^2\right). \tag{27}
$$

Similarly, $\sqrt{P_B}\gamma_B^R$ is approximated to follow a Gaussian distribution whose mean and variance are given as

$$
\mu_2 = L\sqrt{P_B pl(d_{B,I_B})pl(d_{I_B,N_R})}\frac{\pi}{2}\sigma_{Ray}^2
$$

$$
\sigma_2^2 = P_B\left(Lpl(d_{B,I_B})pl(d_{I_B,N_R})\frac{16-\pi^2}{4}\sigma_{Ray}^4 + pl(d_{B,N_R})\sigma_{Ray}^2\right). \tag{28}
$$

From (13), we can notice that $\mu_1 = \mu_2 = \mu$. Now, we derive the required distribution, f_Γ, which is the minimum of two independent Gaussian random variables, $\sqrt{P_A}\gamma_A^R$ and $\sqrt{P_B}\gamma_B^R$; the probability density function (PDF) of Γ can be given as [39]

$$
f_\Gamma(\Gamma) = \frac{1}{\sigma_1}\phi\left(\frac{\Gamma-\mu}{\sigma_1}\right)\Phi\left(-\frac{\Gamma-\mu}{\sigma_2}\right) + \frac{1}{\sigma_2}\phi\left(\frac{\Gamma-\mu}{\sigma_2}\right)\Phi\left(-\frac{\Gamma-\mu}{\sigma_1}\right), \tag{29}
$$

where ϕ and Φ are the PDF and cumulative distribution function (CDF) of the standard normal distribution. Finally, the probability of error can be given as

$$
P_{e_{avg}} = \int_0^\infty P_e(\Gamma)f_\Gamma(\Gamma)d\Gamma, \tag{30}
$$

where $P_e(\Gamma)$ and $f_\Gamma(\Gamma)$ are substituted as in (20) and (29). $P_e(\Gamma)$ is a function of λ_1 and λ_2, and both are functions of Γ as in (17). The integral in (30) does not have a closed-form expression, however, it can be easily computed numerically.

IV. PHASE SHIFTS OPTIMIZATION OF A SINGLE-IRS-PNC

In contrast to the previous sections, in this section, we discuss a TWRC system model that is aided by only one IRS panel seen by the two end nodes. This limitation requires a proper adjustment of the IRS phase shifts to align the two signals from the two end nodes at the relay. The received signal at the relay node, in this case, can be given as

$$
\begin{aligned}
y_R = &\left(\sum\nolimits_{i=1}^L h_{Ai}e^{j\theta_i}g_i + v_A\right)\sqrt{P_A}x_A + \\
&\left(\sum\nolimits_{i=1}^L h_{Bi}e^{j\theta_i}g_i + v_B\right)\sqrt{P_B}x_B + n,
\end{aligned}
\tag{31}
$$

where g_i is the Rayleigh channel fading coefficient between the i-th reflecting element of the IRS panel and the relay node and they follow the channel model in (1). The transmit powers P_A and P_B are adjusted as in (13). Our objective in this section is to calculate the optimum IRS phase shifts, θ_i's, that maximize the amplitude of the received signals at the relay while adhering to the constraint that the two signals are *closely* aligned, i.e., the two received signals must have nearly the same composite magnitude and phase of their respective effective channels at the relay. Hence, this optimization problem can be formulated as

$$
\max_{w_i} \quad \left|\sum\nolimits_{i=1}^L h_{Ai}g_i w_i + v_A\right|^2 \tag{32a}
$$

$$
\text{s.t.} \quad \left|\sqrt{P_A}(\sum\nolimits_{i=1}^L h_{Ai}g_i w_i + v_A) - \sqrt{P_B}(\sum\nolimits_{i=1}^L h_{Bi}g_i w_i + v_B)\right|^2 \le \epsilon \tag{32b}
$$

$$
|w_i| = 1, \quad i = 1, 2, \ldots, L, \tag{32c}
$$

where $w_i = e^{j\theta_i}$ is the reflecting coefficient of the i-th reflector of the IRS panel and ϵ is a relatively small positive number that ensures sufficient alignment of the two received signals, i.e., both signals have nearly same phase and equal amplitudes at the relay. In case we put $\epsilon = 0$, then the constraint becomes an equality constraint which forces the two received signals to have *exactly* same phase and amplitudes at the relay.

The unity absolute value constraints on the IRS coefficients, w_i, restricts the solution of the above optimization problem to be on the surface of a smooth Riemannian manifold contained in $\mathbb{C}^L$. Specifically, all the optimization variables, w_i, are restricted to lie on a continuous search space specified by the complex circle manifold, which is given by

$$
\mathcal{S} = \{w_i \in \mathbb{C} : |w_i| = 1\}. \tag{33}
$$

The circle, $\mathcal{S}$, is a smooth Riemannian sub-manifold of $\mathbb{C}$. The L optimization variables, w_i's, of the IRS have a feasible set which is the Cartesian product of L complex circles, i.e.,

$$
\mathcal{S}_1 \times \mathcal{S}_2 \times \ldots \times \mathcal{S}_L. \tag{34}
$$

The above Cartesian product forms a smooth Riemannian sub-manifold of $\mathbb{C}^L$ because it is the product of smooth Riemannian manifolds. The resultant manifold is called the complex circle manifold and is formally defined as

$$
\mathcal{S}^L = \{\mathbf{w} = [w_1, \cdots, w_L] \in \mathbb{C}^L : |w_1| = \ldots = |w_L| = 1\}. \tag{35}
$$

Therefore, the solution of (32) must be located on the surface of the complex circle manifold. Hence, in the following, we propose a manifold optimization based approach to solve (32). Manifold optimization techniques was used in the IRS literature to solve different problems for different IRS-assisted communication systems [40]–[42].

The optimization problem in (32) has one more constraint in addition to the unit modulus constraints on w_i's. Hence, we propose to use a standard approach to handle the additional constraints which is the exact penalty method. In order to replace the constraints, this method modifies the objective function by adding a weighted penalty for each constraint for violating this constraint. Therefore, the problem is converted to an unconstrained optimization problem, however, a non-smooth one in general. In the Riemannian case, to solve the problem in (32), the exact penalty method solves the following

$$\min_{w_i \in \mathcal{M}} \quad -\left|\sum_{i=1}^{L} h_{Ai} g_i w_i + v_A\right|^2 + \rho \max\left\{0, r(\mathbf{w})\right\}, \quad (36)$$

where $\rho > 0$ is a penalty weight, $\mathcal{M}$ is the Riemannian manifold and $r(\mathbf{w})$ is defined as

$$r(\mathbf{w}) = \left|\sqrt{P_A}(\sum_{i=1}^{L} h_{Ai} g_i w_i + v_A) - \sqrt{P_B}(\sum_{i=1}^{L} h_{Bi} g_i w_i + v_B)\right|^2 - \epsilon. \quad (37)$$

Note that the constant modulus constraint in (32) is satisfied by restricting the feasible set to the manifold $\mathcal{M}$. In the Euclidean case, only a finite penalty weight ρ is needed to exactly satisfy the constraints, hence the method's name. By analogy, we have the same previous approach in the Riemannian manifold case [43]. The resulting penalized cost function in (36) is not smooth because the cost function contains a maximum function that is not smooth around zero. Using a smoothing technique, we can smooth and solve (36) as follows. A common approach called linear-quadratic loss [44] is used to smooth the maximum function in (36). Here, with a smoothing parameter, $u > 0$, we smooth the maximum function as $\max\{0, r(\mathbf{w})\} \approx \mathcal{P}(r(\mathbf{w}), u)$, where $\mathcal{P}(r(w_i), u)$ is given as

$$\mathcal{P}(r(\mathbf{w}), u) = \begin{cases} 0 & r(\mathbf{w}) \leq 0 \\ \frac{r(\mathbf{w})^2}{2u} & 0 \leq r(\mathbf{w}) \leq u \\ r(\mathbf{w}) - \frac{u}{2} & r(\mathbf{w}) \geq u. \end{cases} \quad (38)$$

Therefore, an unconstrained version of our manifold optimization problem can be written as

$$\min_{\mathbf{w} \in \mathcal{M}} \quad Q(\mathbf{w}, \rho, u) = f(\mathbf{w}) + \rho \mathcal{P}(r(\mathbf{w}), u), \quad (39)$$

where $f(\mathbf{w}) = -|\sum_{i=1}^{L} h_{Ai} g_i w_i + v_A|^2 : \mathcal{M} \to \mathbb{R}$ is a smooth real-valued objective function to be optimized. Now, our problem has been converted to a smooth unconstrained optimization on the surface of the complex circle manifold, $\mathcal{S}^L$. Hence, gradient-based unconstrained manifold optimization algorithms can then be used to efficiently search for a solution.

A gradient-descent algorithm on Riemannian manifolds consists of two main steps like the case of Euclidean spaces. At first, we find a descent direction, then the step size along this direction is calculated. These steps are repeated in order to update the solution iteratively until it converges. However, the previous steps are adjusted to cope with the geometric nature

of the manifold and are discussed in the following. The tangent space, $T_{\mathbf{w}}\mathcal{M}$, at a point, $\mathbf{w}$, on a differentiable manifold, $\mathcal{M}$, is defined as the real vector space that intuitively contains the possible directions in which one can tangentially pass through $\mathbf{w}$. The tangent space at $\mathbf{w}$ is given by

$$T_{\mathbf{w}}\mathcal{M} = \{\mathbf{v} \in \mathbb{C}^L : \text{Re}(\mathbf{v} \odot \mathbf{w}^* = \mathbf{0}_L)\}, \quad (40)$$

where $\text{Re}\{\}$ denotes the element-wise real-part of a complex vector, and $\odot$ denotes the Hadamard element-wise multiplication. The gradient that is used in manifold optimization contexts is called the *Riemannian gradient*, and it is the direction of the steepest increase of the cost function at a given point on the manifold, $\mathbf{w}$, but restricted to its tangent space. To compute the Riemannian gradient at a point, we first compute the the Euclidean gradient at this point then we project it onto the tangent space using a projection operator. The projection operator, $P_{T_{\mathbf{w}}\mathcal{M}}$, at point $\mathbf{w}$ on the complex circle manifold is given by [43]

$$P_{T_{\mathbf{w}}\mathcal{M}}(\mathbf{v}) = \mathbf{v} - \text{Re}\{\mathbf{v} \odot \mathbf{w}^*\} \odot \mathbf{w}. \quad (41)$$

Therefore, the Riemannian gradient of our smooth objective function Q on the manifold can be given as

$$\begin{aligned} \nabla_{\mathcal{M}} Q(\mathbf{w}) &= P_{T_{\mathbf{w}}\mathcal{M}}(\nabla Q(\mathbf{w})) \\ &= \nabla Q(\mathbf{w}) - \text{Re}\{\nabla Q(\mathbf{w}) \odot \mathbf{w}^*\} \odot \mathbf{w}, \quad (42) \end{aligned}$$

where $\nabla Q(\mathbf{w})$ is the Euclidean gradient at the point $\mathbf{w}$.

Algorithm 1 presents the steps of solving the unconstrained problem Q in (39) by iteratively updating the penalty coefficient ρ and smoothing parameter u.

Algorithm 1: Exact penalty method via smoothing

---

1 **Input:** Starting point $\mathbf{w}_0$, starting penalty coefficient ρ_0, starting smoothing accuracy u_0, minimum smoothing accuracy $u_{\min}$, constants $\theta_u \in (0, 1)$, $\theta_\rho > 1$, $\tau \geq 0$, minimum step length $d_{\min}$.

2 **for** $k = 0, 1, 2, \ldots$ **do**

3   To obtain $\mathbf{w}_{k+1}$, choose any sub-solver to approximately solve

$$\min_{\mathbf{w} \in \mathcal{M}} \quad Q(\mathbf{w}, \rho_k, u_k)$$

     with warm-start at $\mathbf{w}_k$ and stopping criterion

$$\|\text{grad } Q(\mathbf{w}, \rho_k, u_k)\| \leq \delta.$$

4   **if** $(\text{dist}(\mathbf{w}_k, \mathbf{w}_{k+1}) < d_{\min}$ or $u_k \leq u_{\min})$ and $r(\mathbf{w}_{k+1}) < \tau$ **then**

5   Return $\mathbf{w}_{k+1}$;

6   **end**

7      $u_{k+1} = \max\{u_{\min}, \theta_u u_k\}$;

8   **if** $(k = 0$ or $r(\mathbf{w}_{k+1}) \geq \tau)$ **then**

9         $\rho_{k+1} = \theta_\rho \rho_k$

10   **else**

11         $\rho_{k+1} = \rho_k$;

12   **end**

13 **end**

To sum up, the feasibility of (32) is ensured as follows. The unit modulus constraint in (32c) is simply met by solving the optimization problem on the complex circle manifold as explained above. The other constraint (32b) is satisfied using the exact penalty method as in (36), by stitching the constraint into the objective function itself using a penalty weight, ρ, to convert the problem from being constrained to being an unconstrained optimization problem.

In this paragraph, we discuss the dynamics of **Algorithm 1** and how the parameters ρ and u are updated in each iteration. First, it should be noted that the optimum points of the penalized unconstrained problem in (39) coincide with the optimum points of the original problem if the penalty coefficient ρ is set above some certain threshold [43]. This threshold is often not known and starting with a high value for ρ may slow down the convergence of **Algorithm 1**. Therefore, a common approach in [45] is used to tackle this by setting ρ at a relatively low initial value, then keeping increasing ρ in each iteration if the constraint (32b) is not satisfied as in lines 8 and 9 in **Algorithm 1**. The value τ is set as a low positive number which represents a tolerance factor over which the constraint $r(\mathbf{w}_{k+1})$ is considered out of the feasible set and ρ must be increased. The parameter ρ_k is increased by multiplying it with θ_ρ which is a constant and greater than one. The lower the smoothing parameter u_k, the more approximation accuracy of the function (38). However, if u_k is too small, numerical difficulties may arise in the used approximation function (38). Therefore, the algorithm starts with an initial value u_0, then it decreases the value of u_k in each iteration as in line 7 until it reaches a minimum value $u_{\min}$ after which the value of u_k cannot be decreased. The parameter θ_u is a positive constant fraction which is multiplied by u_k in each iteration to lower its value. When the distance between the obtained solutions in the current and previous iteration is lower than $d_{\min}$, the algorithm terminates. In each iteration, a manifold optimization solver is used to solve the unconstrained problem in (39), as in line 3 in the algorithm, with a stopping criterion set on the gradient norm. We used the trust region solver [43] in the *Manopt* MATLAB tool [46] to solve the manifold optimization problem in each iteration.

V. IRS-PNC FOR HIGHER MODULATION ORDERS

In this section, we study the application of IRS-aided PNC discussed above in practical communication systems where channel coding and higher modulation orders are used. As discussed in previous sections, IRS is used to align the two received superimposed signals and to cancel the CPO problem between the two end nodes. Consequently, the real dimension of one complex signal will remain orthogonal to the imaginary dimension of the other superimposed signal at the relay, and no interference from real dimensions to imaginary dimensions will occur, and vice versa. Therefore, the real dimensions of the two end nodes will be superimposed on each other, separated from the received superimposed imaginary dimensions. Hence, the relay can deduce network-coded packets from both real and imaginary dimensions separately. Therefore, we assume that the information sequence at the end node A is

divided into two streams; $\mathbf{u}_A$ and $\mathbf{u}'_A$. The two information streams are encoded separately using two separate encoders to form the two codewords, $\mathbf{c}_A$ and $\mathbf{c}'_A$. Then, the codeword $\mathbf{c}_A$ is modulated over the real dimension of node A, while $\mathbf{c}'_A$ is modulated over the imaginary dimension to form the modulation-coded complex sequence, $\mathbf{x}_A$. The encoding and modulation at node B is done likewise. Hence, after passing through the IRS-aided TWRC during the broadcast phase, the received vector at the relay is given as

$$\mathbf{y}_R = \Gamma \mathbf{x}_A + \Gamma \mathbf{x}_B + \mathbf{n}_R, \qquad (43)$$

where $\mathbf{n}_R$ is the additive noise vector at the relay N_R and Γ represents the summation of the IRS-adjusted fading channels between the end nodes and the relay in (10)[4]. We consider the RA channel coding in this section, where we design specific decoding schemes to decode the desired network-coded information packets. In the following, the encoding and modulation processes of the channel-coded IRS-assisted PNC design with high modulation orders are illustrated in detail along with their associated decoding schemes.

Denote the q-ary first part, to be modulated on the real dimension, of the information sequence of node m by $\mathbf{u}_m = [u_{m,1}, u_{m,2}, \ldots, u_{m,K}]^T$, $m \in \{A, B\}$, where $u_{m,k} \in \{0, 1, \ldots, q - 1\}$, $k = 1, \ldots, K$, $q = 2^z$, where z is a positive integer and K is the length of the message sequence. The message sequence of node m is encoded to create the codeword, $\mathbf{c}_m = [c_{m,1}, \ldots, c_{m,N}]^T$, using an RA encoder over the ring $R = \mathbb{Z}/q\mathbb{Z}$, where $\mathbb{Z}$ is the set of integer numbers and N is the length of the codeword. The sum operation, $\bar{x} + \bar{y}$, in $\mathbb{Z}/q\mathbb{Z}$ is defined as the remainder when the integer $x + y$ is divided by q. The q-ary codeword, $\mathbf{c}_m$, is then modulated as a real q-pulse amplitude modulation (PAM) signal on the real dimension. Furthermore, the second part of the data sequence, to be modulated on the imaginary dimension, $\mathbf{u}'_m$, is RA-encoded to form the codeword, $\mathbf{c}'_m$, then modulated as a q-PAM signal on the imaginary dimension. Hence, q^2-ary *quadrature amplitude modulation (QAM)* is considered here where the q^2-ary QAM set under consideration is the *Cartesian product* of the real q-PAM signal with itself[5]. The modulation-coded symbol sequence can then be written as $\mathbf{x}_m = [x_{m,1}, \ldots, x_{m,N}]^T$, where $x_{m,n}$ is given by

$$x_{m,n} = \eta \left(c_{m,n} - \frac{q-1}{2} \right) + \eta\, j \left(c'_{m,n} - \frac{q-1}{2} \right), \quad (44)$$

where $m \in \{A, B\}$, $n = 1, 2, \ldots, N$, $j = \sqrt{-1}$, and η is a power scaling factor. In the following, we present two different decoding schemes to decode network-coded information sequences from the received superimposed signal at the relay. In the following, we discuss two decoding schemes, namely modular-sum and arithmetic-sum, to decode the superimposed codewords on the real dimension of the received signal; The decoding of the imaginary dimension is done likewise.

---

[4]Note that channel coded IRS-assisted PNC can be applied to the two-IRS and the single-IRS scenarios which were discussed in II and IV, respectively

[5]For clarity, we present only the case of square QAM constellations. However, our model can be readily extended to non-square constellations.
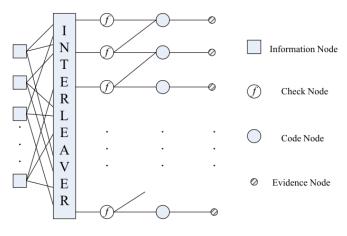
Figure 2: Factor graph for decoding network-coded data packets

A. Modular-Sum-based Channel-Network Decoding

The modular-sum joint channel-network decoding is based on the detection of the R-modulo-sum over the ring, R, of the two signals coming from the end nodes. The relay, N_R, first estimates the probability mass function (PMF) of $c_{A,n} \oplus c_{B,n}$, denoted by $P_{c_{A,n} \oplus c_{B,n}}(a) = \Pr(c_{A,n} \oplus c_{B,n} = a | \mathrm{Re}\{y_{R,n}\})$, from the n-th received symbol $y_{R,n}$, where $\oplus$ is the R-modulo-sum operation defined earlier. Using the same linear channel codes at both end nodes, the sequence $\mathbf{c}_A \oplus \mathbf{c}_B$ is the codeword of $\mathbf{u}_A \oplus \mathbf{u}_B$. By decoding the estimate of $\mathbf{c}_A \oplus \mathbf{c}_B$, i.e. $P_{c_{A,n} \oplus c_{B,n}}$, directly with a soft input decoder, the relay can obtain $\mathbf{u}_A \oplus \mathbf{u}_B$.

The Tanner graph shown in Fig. 2 is read from the left to the right in the RA encoding process, with the function, f, defined as the R-modulo-sum of its two inputs; The output of f can be written as

$$c_{\oplus,n} = f(c_{\oplus,n-1}, s_{\oplus,n}) = c_{\oplus,n-1} \oplus s_{\oplus,n}, \qquad (45)$$

where $c_{\oplus,n} = c_{A,n} \oplus c_{B,n}$, $c_{\oplus,n-1} = c_{A,n-1} \oplus c_{B,n-1}$, and $s_{\oplus,n} = s_{A,n} \oplus s_{B,n}$. The value $s_{m,n}$ is the n-th interleaved symbol of node m, and it equals the value of the k-th information symbol of node m, i.e., $s_{m,n} = u_{m,k}$, where $m \in \{A, B\}$. The mapping from index k to the index n is determined by the interleaver in Fig. 2, which is the same for both of the end nodes' encoders. In the decoding process, input is added to the evidence nodes on the rightmost as q-state message. Then, the messages at the evidence nodes are passed iteratively between the information nodes and code nodes; This process is called belief propagation (BP). The messages on the edges connecting information nodes with check nodes are the PMFs of $u_{\oplus,k} = u_{A,k} \oplus u_{B,k}$, while the messages on the edges connecting the code nodes with the check nodes or the evidence nodes are the PMFs of $c_{\oplus,n} = c_{A,n} \oplus c_{B,n}$. By assuming that the message space is 4-ary, i.e. $q = 4$ and $u_{m,k} \in \{0, 1, 2, 3\}$, as an *example* for the rest of the section, the decoding algorithm is presented in the following steps.

Initialization: Let $\mathbf{p} = (p_0, p_1, p_2, p_3)$ and $\mathbf{q} = (q_0, q_1, q_2, q_3)$ be the input messages to a node that come from two different nodes. The messages on all the edges are initially set to be $(1/4, 1/4, 1/4, 1/4)$ except for the messages on the rightmost edges that are connected to the evidence nodes.

Input of the Evidence Nodes: The messages that are passed from the evidence nodes are the input messages of the decoding algorithm. These messages contain the four-state probabilities of the modulo-4 sum of the two received superimposed codeword symbols, $c_{\oplus,n}$. Denote the input to the n-th evidence node by $\mathbf{p}_n = (p_0, p_1, p_2, p_3)$. Given the observation at the relay node, the likelihood function of $c_{\oplus,n}$ can be written as

$$g_1(R_A, R_B) = \frac{1}{\beta_1} \exp\left\{ \frac{-(\mathrm{Re}\{y_{R,n}\} - \Gamma R_A - \Gamma R_B)^2}{2\sigma^2} \right\}, \quad (46)$$

while the likelihood function of $c'_{\oplus,n} = c'_{A,n} \oplus c'_{B,n}$, when decoding the imaginary dimension, can be written as

$$g_2(I_A, I_B) = \frac{1}{\beta_2} \exp\left\{ \frac{-(\mathrm{Im}\{y_{R,n}\} - \Gamma I_A - \Gamma I_B)^2}{2\sigma^2} \right\}, \quad (47)$$

where $R_A = \mathrm{Re}\{x_{A,n}\}$, $R_B = \mathrm{Re}\{x_{B,n}\}$, $I_A = \mathrm{Im}\{x_{A,n}\}$, $I_B = \mathrm{Im}\{x_{B,n}\}$, σ^2 is the variance of the real or imaginary dimension of the complex noise. Assuming that $\eta = 2$ in (44), then the codeword elements are mapped to $\{-3, -1, 1, 3\}$ on the real and imaginary parts of $x_{m,n}$. In this case, we specify the input probabilities to the evidence node as

$$
\begin{aligned}
p_0 &= g_x(-3, -3) + g_x(1, 1) + g_x(3, -1) + g_x(-1, 3) \\
p_1 &= g_x(-3, -1) + g_x(-1, -3) + g_x(3, 1) + g_x(1, 3) \\
p_2 &= g_x(3, 3) + g_x(-1, -1) + g_x(-3, 1) + g_x(1, -3) \\
p_3 &= g_x(1, -1) + g_x(-1, 1) + g_x(3, -3) + g_x(-3, 3), \quad (48)
\end{aligned}
$$

where $x \in \{1, 2\}$ and β_x is a normalization factor that ensures that $\sum_{i=0}^{3} p_i = 1$.

Message Updating at the variable Nodes: The variable nodes in Fig. 2 are the code nodes and information nodes. Assuming that the repetition factor of the RA encoder is 3, every variable node is connected to three separate edges except for the last code node at the bottom of the factor graph in Fig. 2. The output message of a variable node is represented as $VAR(\mathbf{p}, \mathbf{q})$, where $\mathbf{p}$ and $\mathbf{q}$ are the input messages passed from the other two connected edges, whereas the output is the updated message on the rest edge. Using the same probability calculations in [47], the output message for the variable node is obtained as

$$VAR(\mathbf{p}, \mathbf{q}) = \frac{1}{\zeta}(p_0 q_0, p_1 q_1, p_2 q_2, p_3 q_3), \qquad (49)$$

where ζ is a normalization factor which ensures that $\frac{1}{\zeta} \sum_{i=0}^{3} p_i q_i = 1$.

Message Updating for the Check Nodes: Designing the message updating rules for the check nodes is one of the core concerns in the sum-product decoding algorithm applied in PNC. As we see in Fig. 2, every check node is connected to three edges except for the first check node at the top of the graph. The output message of a check node is represented as $CHK(\mathbf{p}, \mathbf{q})$, where $\mathbf{p}$ and $\mathbf{q}$ are the input messages that come from the other two connected edges, whereas the output is the updated message on the third (rest) edge. Now, we compute the message updating rules at the check node in both backward and forward propagation. First, we compute the output message of the check node when propagating from right to left, i.e. backward propagation, during the BP algorithm. Let

$S = s_{\oplus,n}$, $\bar{C} = c_{\oplus,n-1}$, and $C = c_{\oplus,n}$, the probability that the symbol S is equal to 0 given the two input messages $\mathbf{p}$ and $\mathbf{q}$ is calculated, given that $C = S \oplus \bar{C}$, as

$$\Pr(S = 0|\bar{C} \sim \mathbf{p}, C \sim \mathbf{q})$$
$$= \sum_{i=0}^{3} \Pr(\bar{C} = i)\Pr(S = 0|\bar{C} = i, C \sim \mathbf{q})$$
$$= \Pr(\bar{C} = 0|\mathbf{p})\Pr(C = 0|\mathbf{q}) + \Pr(\bar{C} = 1|\mathbf{p})\Pr(C = 1|\mathbf{q})$$
$$+ \Pr(\bar{C} = 2|\mathbf{p})\Pr(C = 2|\mathbf{q}) + \Pr(\bar{C} = 3|\mathbf{p})\Pr(C = 3|\mathbf{q})$$
$$= p_0 q_0 + p_1 q_1 + p_2 q_2 + p_3 q_3, \tag{50}$$

where $C \sim \mathbf{q}$ means that the random variable C has a PMF distribution as the values in the $\mathbf{q}$ vector. Similarly, the probabilities that the symbol S takes the values 1, 2, and 3, given the two input messages, can be obtained. Therefore, the message update rule at the check node in the backward propagation is given as

$$CHK_1(\mathbf{p}, \mathbf{q}) = (p_0 q_0 + p_1 q_1 + p_2 q_2 + p_3 q_3,$$
$$p_0 q_1 + p_1 q_2 + p_2 q_3 + p_3 q_0, \ p_0 q_2 + p_1 q_3 + p_2 q_0 + p_3 q_1,$$
$$p_0 q_3 + p_1 q_0 + p_2 q_1 + p_3 q_2). \tag{51}$$

On the other hand, when the message passing is from left to right, i.e. forward propagation, the probability that the symbol C is equal to 0 given the two input messages $\mathbf{p}$ and $\mathbf{q}$ is calculated, given that $C = S \oplus \bar{C}$, as

$$\Pr(C = 0|\bar{C} \sim \mathbf{p}, S \sim \mathbf{q})$$
$$= \Pr(\bar{C} = 0|\mathbf{p})\Pr(S = 0|\mathbf{q}) + \Pr(\bar{C} = 1|\mathbf{p})\Pr(S = 3|\mathbf{q})$$
$$+ \Pr(\bar{C} = 2|\mathbf{p})\Pr(S = 2|\mathbf{q}) + \Pr(\bar{C} = 3|\mathbf{p})\Pr(S = 1|\mathbf{q}). \tag{52}$$

Similarly, the probabilities that the symbol C takes the values 1, 2, and 3, given the two input messages, can be obtained. Therefore, the message update rule at the check node in the forward propagation is given as

$$CHK_2(\mathbf{p}, \mathbf{q}) = (p_0 q_0 + p_1 q_3 + p_2 q_2 + p_3 q_1,$$
$$p_0 q_1 + p_1 q_0 + p_2 q_3 + p_3 q_2, \ p_0 q_2 + p_1 q_1 + p_2 q_0 + p_3 q_3,$$
$$p_0 q_3 + p_1 q_2 + p_2 q_1 + p_3 q_0). \tag{53}$$

B. Arithmetic-sum based channel-network decoding

In this subsection, and motivated by the results in [47], which show the superiority of arithmetic-sum-based decoding in the binary case over the modulo-2 sum, we consider the use of arithmetic-sum based decoding. We extend the work in [47], which considered only binary channel-coded PNC. We design and present the arithmetic-sum-based channel-network decoding scheme for the general q-ary message sequences. The 4-ary message sequences, i.e. $q = 4$, are considered as an example in this subsection, by deriving its factor graph and the corresponding update rules[6] of the BP decoding algorithm.

The arithmetic-sum based decoding scheme works as follows. First, the relay obtains the PMF of $u_{A,k} + u_{B,k}$, denoted by $P_{u_{A,k}+u_{B,k}}(a) = \Pr(u_{A,k} + u_{B,k} = a|\mathbf{y}_R)$, by decoding the received signal, $\mathbf{y}_R$. The " $+$ " operation here is the regular arithmetic-sum over the real numbers. Then, the target

[6]The design presented here can be readily extended to consider any other higher-order modulation scheme.

network-coded information, $u_A \oplus u_B$, can be directly obtained using the following symbol-level PNC mapping

$$u_{A,k} \oplus u_{B,k} = \begin{cases} 0 & \arg\max P_{u_{A,k}+u_{B,k}}(a) = 0 \text{ or } 4 \\ 1 & \arg\max P_{u_{A,k}+u_{B,k}}(a) = 1 \text{ or } 5 \\ 2 & \arg\max P_{u_{A,k}+u_{B,k}}(a) = 2 \text{ or } 6 \\ 3 & \arg\max P_{u_{A,k}+u_{B,k}}(a) = 3. \end{cases} \tag{54}$$

After that, the network coded information, $\mathbf{u}_A \oplus \mathbf{u}_B$, is encoded at the relay using a standard channel encoder and is broadcast to both end nodes in the broadcast phase.

The decoder at N_R is different from the traditional RA decoder. In arithmetic-sum based PNC, the decoder can be considered as processing the received superimposed vector, $\mathbf{y}_R$, at the relay to produce the arithmetic-sum of the two source message sequences, $\mathbf{u}_A + \mathbf{u}_B$. Without the additive noise at the relay, the received signals are the superposition of the two codewords transmitted by the two end nodes. Hence, the objective of the decoder at N_R can be seen as the inverse of the superposition of the encoding processes at the end nodes. Therefore, the decoder at N_R can be considered as the decoder of a *virtual* encoder whose input $\mathbf{u}_v$ and output $\mathbf{c}_v$ are

$$\mathbf{u}_v = \mathbf{u}_A + \mathbf{u}_B, \qquad \mathbf{c}_v = \mathbf{c}_A + \mathbf{c}_B. \tag{55}$$

The decoder design is based on the structure of this virtual encoder which is similar to that of the regular RA encoder in Fig. 2, when being read form left to right, except that the modulo-q sum is now replaced by a general function f. The function f is derived based on the requirements in (55). Consequently, the function f in Fig. 2 needs to satisfy

$$c_{v,n} = f(c_{v,n-1}, s_{v,n}) = c_{A,n} + c_{B,n}, \tag{56}$$
$$\text{when } u_{v,k} = u_{A,k} + u_{B,k},$$

where the symbol, $s_{v,n} = s_{A,n} + s_{B,n}$, is the n-th interleaved symbol of the virtual encoder, i.e., $s_{v,n} = u_{v,k}$. The mapping from the index k to the index n is determined by the interleaver, which is the same for both the end nodes' encoders and the virtual encoder. Based on Fig. 2, the relations between $c_{A,n}$, $c_{B,n}$ and $u_{A,k}$, $u_{B,k}$ can be, respectively, written as

$$c_{A,n} = c_{A,n-1} \oplus s_{A,n} = c_{A,n-1} \oplus u_{A,k}$$
$$c_{B,n} = c_{B,n-1} \oplus s_{B,n} = c_{B,n-1} \oplus u_{B,k}. \tag{57}$$

By combining equations (56) and (57), the general function f can be obtained as

$$c_{v,n} = f(c_{v,n-1}, s_{v,n}) = c_{A,n-1} \oplus u_{A,k} + c_{B,n-1} \oplus u_{B,k}, \tag{58}$$

where all possible inputs and corresponding outputs of f are calculated in Table I for a 4-ary message sequence.

In the decoding process of the arithmetic-sum, the input is added to the evidence nodes on the rightmost as a $(2q-1)$-state message, which represents the PMF of the arithmetic-sum, $c_{A,n} + c_{B,n}$. The messages on the edges connecting information nodes with check nodes are the PMFs of $u_{A,k} + u_{B,k}$, while those on the edges connecting the code nodes with the check nodes or the evidence nodes are the PMFs of $c_{A,n} + c_{B,n}$. By assuming the message space is 4-ary, i.e. $q = 4$ and $u_{m,k} \in \{0, 1, 2, 3\}$, as an *example* for the rest of the section, the decoding is presented in the following steps.

$c_{A,n}+c_{B,n}$	$c_{A,n-1}+c_{B,n-1}$	$s_{A,n}+s_{B,n}$	$c_{A,n}+c_{B,n}$	$c_{A,n-1}+c_{B,n-1}$	$s_{A,n}+s_{B,n}$	$c_{A,n}+c_{B,n}$	$c_{A,n-1}+c_{B,n-1}$	$s_{A,n}+s_{B,n}$
4	6	6	3	4	3	2	2	0
3	6	5	2,6	4	2	3	1	6
2	6	4	1,5	4	1	2,6	1	5
1,5	6	3	4	4	0	1,5	1	4
0,4	6	2	1,5	3	6	0,4	1	3
3	6	1	0,4	3	5	3	1	2
6	6	0	3	3	4	2	1	1
3	5	6	2,6	3	3	1	1	0
2	5	5	1,5	3	2	6	0	6
1,5	5	4	0,4	3	1	5	0	5
0,4	5	3	3	3	0	4	0	4
3	5	2	0,4	2	6	3	0	3
2,6	5	1	3	2	5	2	0	2
5	5	0	2,6	2	4	1	0	1
2	4	6	1,5	2	3	0	0	0
1,5	4	5	0,4	2	2	–	–	–
0,4	4	4	3	2	1	–	–	–

Table I: The truth table of the function, f, for the arithmetic sum case

Initialization: Let $\mathbf{p} = (p_0, p_1, p_2, p_3, p_4, p_5, p_6)$ and $\mathbf{q} = (q_0, q_1, q_2, q_3, q_4, q_5, q_6)$ be the message input from two different nodes. All the messages associated with the edges are initially set to the *prior probabilities* of the seven states, i.e. $(1/16, 2/16, 3/16, 4/16, 3/16, 2/16, 1/16)$, except for the messages on the edges connected to the evidence nodes.

Input of the Evidence Nodes: Denote the input seven-state PMF of $c_{A,n} + c_{B,n}$ at the n-th evidence node as $\mathbf{p}_n = (p_0, p_1, p_2, p_3, p_4, p_5, p_6)$, which is calculated as

$$p_0 = g_x(-3, -3), \ p_1 = g_x(-3, -1) + g_x(-1, -3),$$
$$p_2 = g_x(-1, -1) + g_x(-3, 1) + g_x(1, -3),$$
$$p_3 = g_x(1, -1) + g_x(-1, 1) + g_x(3, -3) + g_x(-3, 3),$$
$$p_4 = g_x(1, 1) + g_x(-3, 1) + g_x(1, -3),$$
$$p_5 = g_x(3, 1) + g_x(1, 3), \ p_6 = g_x(3, 3), \tag{59}$$

where $x \in \{1, 2\}$, g_x is defined in (46) and (47) in which β_x is a normalization factor that ensures that $\sum_{i=0}^{6} p_i = 1$.

Message Updating for the variable Nodes: Assuming that the repetition factor of the *virtual* RA encoder is 3, every variable node is connected to three separate edges except for the last code node at the bottom. The output message of a variable node is represented as $VAR(\mathbf{p}, \mathbf{q})$, where $\mathbf{p}$ and $\mathbf{q}$ are the seven-state input messages passed from the other two connected edges, whereas the output is the updated message on the rest edge. Using the same calculations in [47], the output message for the variable node in our scheme is derived as

$$VAR(\mathbf{p}, \mathbf{q}) = \frac{1}{\zeta}\left(p_0 q_0, \frac{p_1 q_1}{2}, \frac{p_2 q_2}{3}, \frac{p_3 q_3}{4}, \frac{p_4 q_4}{3}, \frac{p_5 q_5}{2}, p_6 q_6\right), \tag{60}$$

where ζ is a normalization factor.

Message Updating for the Check Nodes: The output message of a check node is represented as $CHK(\mathbf{p}, \mathbf{q})$, where $\mathbf{p}$ and $\mathbf{q}$ are the input messages that come from the other two connected edges, whereas the output is the updated message on the third (rest) edge. Let $S = s_{A,n} + s_{B,n}$, $\bar{C} = c_{A,n-1} + c_{B,n-1}$, and $C = c_{A,n} + c_{B,n}$, we first compute the output message of the check node when propagating from right to left (backward propagation), i.e., the PMF of S. The PMF of S is derived by calculating the probabilities that S takes the values $0, 1, \ldots, 6$

given the PMFs of C and $\bar{C}$. The probability that the symbol S is equal to 0 given $\mathbf{p}$ and $\mathbf{q}$ is calculated as

$$\Pr(S{=}0|\bar{C}{\sim}\mathbf{p}, C{\sim}\mathbf{q}) = \sum_{i=0}^{6} \Pr(\bar{C}{=}i|\mathbf{p})\Pr(S{=}0|\bar{C}{=}i, C{\sim}\mathbf{q}). \tag{61}$$

To calculate $\Pr(S{=}0|\bar{C}{=}i, C{\sim}\mathbf{q})$, let's take an example when $\bar{C} = 2$. From Table I, given $\bar{C} = 2$, we can find that $S = 0$ or 4 when $C = 2$. Hence, we need to calculate how probable $S = 0$ is when $C = 2$ given that $\bar{C} = 2$. From (58), we can obtain all the possibilities that C takes the value 2 when $\bar{C} = 2$. When $\bar{C} = 2$, the pair $(c_{A,n-1}, c_{B,n-1})$ can take the values $(0, 2), (2, 0), (1, 1)$. When $S = 0$, the pair $(s_{A,n}, s_{B,n})$ takes the value $(0, 0)$, however, when $S = 4$, the pair can take the values $(2, 2), (3, 1)$, or $(1, 3)$; using these values in (58) and taking all possible combinations that lead to $C = 2$ as in Table II, we can count the number of occurrences of $S{=}0$ when $\bar{C}{=}2$ and $C{=}2$.

From Table II, we see that $S{=}s_{A,n}{+}s_{B,n}$ took the value 0 three times out of nine when $C{=}2$. Hence, the probability $\Pr(S{=}0|\bar{C}{=}i, C{\sim}\mathbf{q})$ equals to $(1/3)\Pr(C{=}2){=}(1/3)q_2$. In a similar manner, we can get the other terms of (61) as

$$\Pr(S = 0|\bar{C} \sim \mathbf{p}, C \sim \mathbf{q})$$
$$= \Pr(\bar{C}{=}0|\mathbf{p})\Pr(C{=}0|\mathbf{q}) + (1/2)\Pr(\bar{C}{=}1|\mathbf{p})\Pr(C{=}1|\mathbf{q})$$
$$+ (1/3)\Pr(\bar{C}{=}2|\mathbf{p})\Pr(C{=}2|\mathbf{q}) + (1/4)\Pr(\bar{C}{=}3|\mathbf{p})\Pr(C{=}3|\mathbf{q})$$
$$+ (1/3)\Pr(\bar{C}{=}4|\mathbf{p})\Pr(C{=}4|\mathbf{q}) + (1/2)\Pr(\bar{C}{=}5|\mathbf{p})\Pr(C{=}5|\mathbf{q})$$
$$+ \Pr(\bar{C}{=}6|\mathbf{p})\Pr(C{=}6|\mathbf{q})$$
$$= p_0 q_0 + \frac{p_1 q_1}{2} + \frac{p_2 q_2}{3} + \frac{p_3 q_3}{4} + \frac{p_4 q_4}{3} + \frac{p_5 q_5}{2} + p_6 q_6. \tag{62}$$

Similarly, the probabilities that the symbol S takes the values $1, \ldots, 6$ given the two input messages can be calculated. Therefore, the message update rule at the check node in backward propagation can be given as in (63).

When the messages are passed form left to right, i.e., during forward propagation, the probability that the symbol C is equal

11

C	$c_{A,n-1}$	$s_{A,n}$	$c_{B,n-1}$	$s_{B,n}$
2	0	0	2	0
2	2	0	0	0
2	1	0	1	0
2	0	2	2	2
2	2	2	0	2
6	1	2	1	2
6	0	3	2	1
2	2	3	0	1
2	1	3	1	1
2	0	1	2	3
6	2	1	0	3
2	1	1	1	3

Table II: Possible combinations of the backward example

C	$c_{A,n-1}$	$s_{A,n}$	$c_{B,n-1}$	$s_{B,n}$
0	0	0	2	2
4	2	0	0	2
4	1	0	1	2
4	0	2	2	0
0	2	2	0	0
4	1	2	1	0
4	0	1	2	1
4	2	1	0	1
4	1	1	1	1

Table III: Possible combinations of the forward example

VI. SIMULATION RESULTS

In this section, the performance of both PNC scenarios aided with two IRS panels, and only one IRS panel is evaluated to show the significance of optimizing the IRS reflectors to align the two received signals at the relay. Additionally, the performance of the proposed channel coded IRS-PNC with high modulation orders is evaluated. With this simulation, we evaluate the designed channel coded PNC scheme and prove the convergence of the calculated update rules of the BP decoding of both modular sum and arithmetic sum based channel coded PNC schemes. We are interested in evaluating the error performance of the detected network-coded signal at the relay as it represents the bottleneck of the PNC system.

In this simulation study, we assume a general unbalanced channels case where node A is closer to the relay than node B. For all the figures, except Fig. 4, the node-IRS, IRS-relay and node-relay distances for node A are assumed as $d_{A,I_A} = 30$, $d_{I_A,N_R} = 30$ and $d_{A,N_R} = 50$, while these distances are $d_{B,I_B} = 60$, $d_{I_B,N_R} = 60$ and $d_{B,N_R} = 100$ for node B, respectively. Moreover, the transmit powers of the two nodes, P_A and P_B, are adjusted according to (13) to compensate for the unbalanced channel gains of the two nodes. The path loss at the reference distance in (3) is $\eta_0 = 10^{-3}$, and the path loss exponents for the direct links (node-relay), node-IRS links and IRS-relay links are assumed as $\alpha_d = 5.5$, $\alpha_{N,I} = 2.2$ and $\alpha_{I,R} = 2.2$, respectively. The noise power σ_n^2 is set to be -114 dBm.

Fig. 3 compares the performances of the different PNC detectors against the proposed simplified PNC detector in Sec. III-B for the uncoded double-IRS PNC scenario. The comparison is done for different values of the number of

to 0 given $\mathbf{p}$ and $\mathbf{q}$ is calculated, following Table I, as

$\Pr(C = 0|\bar{C} \sim \mathbf{p}, S \sim \mathbf{q})$
$= \Pr(\bar{C}{=}0|\mathbf{p})\Pr(S{=}0|\mathbf{q}) + (1/4)\Pr(\bar{C}{=}1|\mathbf{p})\Pr(S{=}3|\mathbf{q})$
$+(2/9)\Pr(\bar{C}{=}2|\mathbf{p})\Pr(S{=}2|\mathbf{q}) + (1/3)\Pr(\bar{C}{=}2|\mathbf{p})\Pr(S{=}6|\mathbf{q})$
$+(1/4)\Pr(\bar{C}{=}3|\mathbf{p})\Pr(S{=}1|\mathbf{q}) + (1/4)\Pr(\bar{C}{=}3|\mathbf{p})\Pr(S{=}5|\mathbf{q})$
$+(1/3)\Pr(\bar{C}{=}4|\mathbf{p})\Pr(S{=}4|\mathbf{q}) + (1/4)\Pr(\bar{C}{=}5|\mathbf{p})\Pr(S{=}3|\mathbf{q})$
$+(1/3)\Pr(\bar{C}{=}6|\mathbf{p})\Pr(S{=}2|\mathbf{q})$
$= p_0 q_0 + p_1 q_3/4 + p_2(q_6/3 + 2q_2/9) + p_3(q_5 + q_1)/4$
$+ p_4 q_4/3 + p_5 q_3/4 + p_6 q_2/3.$ (65)

In (65), we have accounted for all combinations of $\bar{C}$ and S that produce $C = 0$. However, sometimes, e.g. $(\bar{C}, S){=}(2,2)$, C may be 0 or 4. In this case, we have to compute the probability of $C{=}0$ when $(\bar{C}, S){=}(2,2)$. When $\bar{C}{=}2$, the pair $(c_{A,n-1}, c_{B,n-1})$ can take the values $(0,2), (2,0)$, or $(1,1)$. When $S = 2$, the pair $(s_{A,n}, s_{B,n})$ can take the values $(0,2), (2,1)$, or $(1,1)$; using these values in (58) and taking all possible combinations as in Table III, we can count the number of occurrences of $C{=}0$ when $\bar{C}{=}2$ and $S{=}2$.

From Table III, we see that $C{=}0$ occurred two times out of the nine possibilities. Hence, the probability $\Pr(C{=}0|\bar{C}{=}2, S{=}2)$ is 2/9. Similarly, we can get the scaling fractions of the other terms in (65).

The probabilities that the symbol C takes the values $1, \ldots, 6$ given the two input messages, can be calculated in the same manner. Therefore, the message update rule at the check node in the forward propagation can be given as in (64).

$CHK_1(\mathbf{p}, \mathbf{q}) = [p_0 q_0 + p_1 q_1/2 + p_2 q_2/3 + p_3 q_3/4 + p_4 q_4/3 + p_5 q_5/2 + p_6 q_6,$
$\quad p_0 q_1 + 2p_1 q_2/3 + p_2 q_3/2 + p_3(q_0 + q_4)/2 + p_4(q_1/3 + 2/3q_5) + p_5(q_2/3 + q_6) + p_6 q_3/2,$
$\quad p_0 q_2 + 3p_1 q_3/4 + p_2(2q_0/3 + 7q_4/9) + 3p_3(q_1 + q_5)/4 + p_4(2q_2/3 + q_6) + 3p_5 q_3/4 + p_6(q_0 + 2q_4/3),$
$\quad p_0 q_3 + p_1(q_0 + q_4) + p_2(q_1 + q_5) + p_3(q_2 + q_6) + p_4 q_3 + p_5(q_0 + q_4) + p_6(q_1 + q_5),$
$\quad p_0 q_4 + p_1(q_1/2 + q_5) + p_2(2q_2/3 + q_6) + 3p_3 q_3/4 + p_4(q_0 + 2q_4/3) + p_5(q_1 + q_5/2) + p_6 q_2,$
$\quad p_0 q_5 + p_1(q_2/3 + q_6) + p_2 q_3/2 + p_3(q_0 + q_4)/2 + p_4(2q_1/3 + q_5/3) + 2p_5 q_2/3 + p_6 q_3/2,$
$\quad p_0 q_6 + p_1 q_3/4 + p_2(q_0/3 + 2q_4/9) + p_3(q_1 + q_5)/4 + p_4 q_2/3 + p_5 q_3/4 + p_6 q_4/3]$ (63)

$CHK_2(\mathbf{p}, \mathbf{q}) = [p_0 q_0 + p_1 q_3/4 + p_2(q_6/3 + 2q_2/9) + p_3(q_5 + q_1)/4 + p_4 q_4/3 + p_5 q_3/4 + p_6 q_2/3,$
$\quad p_0 q_1 + p_1(q_0 + q_4/3) + p_2 q_3/2 + p_3(q_6 + q_2)/2 + p_4(2q_5/3 + q_1/3) + 2p_5 q_4/3 + p_6 q_3/2,$
$\quad p_0 q_2 + p_1(q_1 + q_5/2) + p_2(q_0 + 2q_4/3) + 3p_3 q_3/4 + p_4(2q_2/3 + q_6) + p_5(q_1/2 + q_5) + p_6 q_4,$
$\quad p_0 q_3 + p_1(q_2 + q_6) + p_2(q_1 + q_5) + p_3(q_0 + q_4) + p_4 q_3 + p_5(q_2 + q_6) + p_6(q_1 + q_5),$
$\quad p_0 q_4 + 3p_1 q_3/4 + p_2(7q_2/9 + 2q_6/3) + 3p_3(q_1 + q_5)/4 + p_4(q_0 + 2q_4/3) + 3p_5 q_3/4 + p_6(q_6 + 2q_2/3),$
$\quad p_0 q_5 + 2p_1 q_4/3 + p_2 q_3/2 + p_3(q_6 + q_2)/2 + p_4(2q_1/3 + q_5/3) + p_5(q_0 + q_4/3) + p_6 q_3/2,$
$\quad p_0 q_6 + p_1 q_5/2 + p_2 q_4/3 + p_3 q_3/4 + p_4 q_2/3 + p_5 q_1/2 + p_6 q_0]$ (64)

12

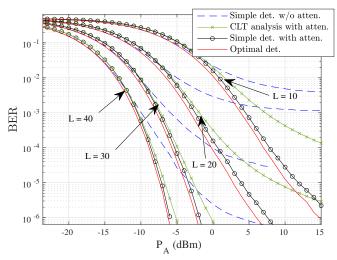Figure 3: Simulation vs. approximate theoretical BER performance of the two-IRS PNC scenario, with different number of reflectors L

Figure 4: BER performance of the one-IRS PNC scenario: optimal phase shifts vs. any random feasible solution

reflector elements at the IRS panels, $L = 10, 20, 30, 40$. Fig. 3 compares the performance of the optimal detector in (8) against the proposed simplified detector with simple thresholds in (17). We plot the performance of the simple detector with and without attenuation control at the IRS to show the advantage of applying the attenuation factors. The figure shows that the proposed simple detector in Sec. III-B with attenuation control at the IRS provides a very close performance to the optimal detector in (8). This proves the efficacy of using the proposed simplified detector with attenuation control at the IRS panels. On the other hand, the graph shows the inferiority of using the simple PNC detector without applying the attenuation factors discussed in Sec. III-B, which proves the importance of applying these attenuation controls at the IRS. Fig. 3 also compares the simulated bit error rate (BER) performance of the proposed simplified PNC detector with IRS attenuation control against the derived CLT-based expression of the approximate detection error probability, derived in Sec. III. We can notice from the figure that the curves plotted using the approximate analytical expression in (30) get closer to the simulated error probability curves as the number of reflectors, L, increases. The reason behind this observation is that as L increases, the CLT-based Gaussian approximation of the sum of the IRS channels becomes tighter and converges to the actual distribution of the sum. Hence, as the CLT approximation gets more accurate, the CLT-based analytical error curves become more accurate and closer to the true error curves plotted using Monte Carlo simulations. The figure also shows that the system's performance enhances as L increases because the number of received signal copies increases in accordance, which improves the received signal quality at the relay.

In Fig. 4, the BER performance of the one-IRS PNC scenario is shown. We assume the distances between the nodes and the IRS panel are $d_{A,I} = 60$ and $d_{B,I} = 60$, while the distance between the IRS and the relay is $d_{I,N_R} = 30$. The BER of the one-IRS scenario with optimized phase-shifts, after solving (32) using **Algorithm 1**, is compared with the one-IRS scenario without optimization over the Riemannian
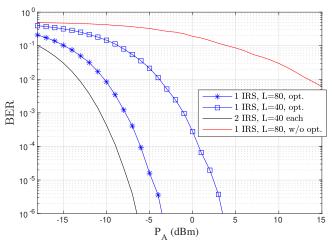
manifold, i.e., using any feasible solution which satisfies the constraint in (32). All feasible points that satisfy this constraint can successfully align the two received superimposed signals, coming from the two end nodes, in the PNC fashion, i.e., to have nearly the same phase and equal amplitudes at the relay. However, not all points in this feasible set can maximize the sum amplitude of the received signals at the relay, $\Gamma_{opt} = |\sum_{i=1}^{L} h_{Ai} g_i w_i^* + v_A|^2$, to minimize the detection error probability of the PNC detector discussed in Sec. III. Therefore, Fig. 4 shows that the performance of the optimized one-IRS scenario with $L = 40, 80$ largely beats that of the one-IRS scenario without optimization. This shows the significance of the phase shifts optimization discussed in Sec. IV. It is also noticeable that the double-IRS scenario with $L = 40$ per each panel outperforms the single-IRS scenario with number of reflectors $L = 40$. This is intuitive since the single-IRS scenario has an extra constraint of *jointly* aligning the two received signals which limits the maximum attainable amplitude at the relay. Whereas, this limiting constraint does not exist in the two-IRS scenario as each end node is served by a separate IRS-panel. Additionally, the figure shows that double-IRS scenario can also outperform the single-IRS scenario even with same total number of reflectors $L = 80$. Although the two end nodes see the whole $L = 80$ reflecting elements in the single-IRS scenario, unlike the double-IRS scenario, still the double-IRS scenario outperforms the single-IRS scenario. The reason behind this is that the IRS panels are placed closer to the end nodes and the relay in the double-IRS scenario, which leads to higher channel gains. In contrast, we can only place the single-IRS in the middle, leading to larger distances from the nodes and hence higher path loss for both nodes. However, the single-IRS scenario is unavoidable to the TWRC system when only one IRS panel is available.

Fig. 5, Fig. 6 and Fig. 7 discuss the performance of channel coded PNC operating in the two-IRS scenario. Fig. 5 and Fig. 6 show the error probability performance of the two-IRS scenario when binary and q-ary channel coded PNC are applied, respectively. However, Fig. 7 focuses on the performance comparison between modulo-q versus arithmetic based channel-network decoding when the q-ary channel coded PNC
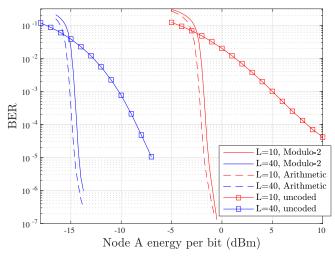
Figure 5: BER of modulo-2 sum vs. arithmetic sum for the case of binary RA-coded PNC in the two-IRS scenario using QPSK

Figure 6: SER of 4-ary uncoded vs. RA-coded PNC, over R_4, using modulo-4 channel-network decoding using 16-QAM

Figure 7: SER performance of modulo-4 sum vs. arithmetic sum for 4-ary RA-coded PNC, over the ring R_4, in the two-IRS scenario

is applied in the two-IRS scenario. The following simulation parameters are unified for the three figures. The data packet length is set to be 2048 and the repetition factor of the RA encoder is set to be 3. For every energy per symbol value, we average the error performance over 10000 data packets which are generated at both end nodes. The relay receives 10000 interfered packets, each representing the sum of the corresponding two packets transmitted simultaneously from the two end nodes.

Fig. 5 shows the BER performance of channel coded PNC in the two-IRS scenario when the two end nodes transmit QPSK signals and compares it to the uncoded PNC case. Each QPSK signal is the Cartesian product of two orthogonal BPSK signals on the real and imaginary dimensions. The message vectors at the end nodes are binary RA-encoded to form the binary codewords which are then BPSK-modulated and transmitted. As discussed before, no interference from the real dimensions to the imaginary dimensions of the two nodes will occur because of the IRS channel adjustment. Hence, the relay decodes the real and imaginary dimensions separately using binary PNC channel-network decoding to get the XOR of the two message vectors of the two end nodes. As shown in Fig. 5, the BER of the detected XOR data at the relay decreases as the number of reflector elements of the IRS panel, L, increases because of the increased number of reflected rays in the case of $L = 40$. The figure shows the significant improvement of channel coded PNC over the uncoded case when the same energy per bit is used for both cases. The figure also shows that arithmetic-based channel-network decoding for IRS-aided PNC outperforms the modulo-2 based decoding, which is consistent with the results in [47] for the binary case.

Fig. 6 shows the symbol error rate (SER) performance of channel coded PNC in the two-IRS scenario when the two end nodes transmit 16-QAM signals, and compares it to the uncoded PNC case. Each 16-QAM signal is the Cartesian product of two orthogonal 4-PAM signals on the real and imaginary dimensions. The message sequences at the end nodes are symbols drawn from the ring R_4. The relay decodes the real and imaginary dimensions separately using 4-ary PNC
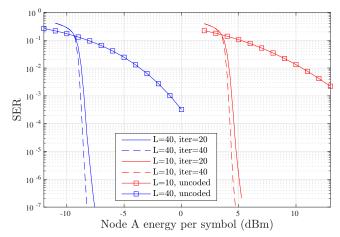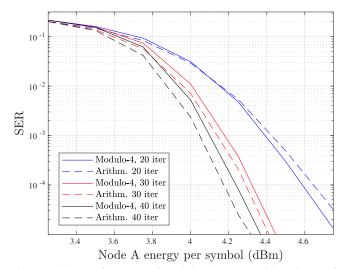
channel-network decoding to get the modulo-4 of the two message vectors of the two end nodes. In Fig. 6, as the number of reflector elements of the IRS panel, L, increases, the SER of the detected modulo-4 data at the relay decreases. The figure shows the significant improvement of 4-ary channel coded PNC over the uncoded 4-ary case when the same level of energy per data symbol is used for both cases. The figure also shows that the SER decreases as the number of iterations of the BP algorithm increases when using the derived update rules in (51) and (53) in the backward and forward propagation.

Fig. 7 compares the performance of modulo-4 sum with arithmetic based sum channel-network decoding when the 4-ary channel coded PNC is applied in the two-IRS scenario. The figure compares the performance of both decoding schemes for a different number of iterations of the BP algorithm. The graph shows that the BER performance of the two schemes is nearly the same at 20 iterations. However, the arithmetic-sum-based decoding provides some performance gain over the modulo-4 sum based one at 30 and 40 iterations. It is noted that the complexity of the arithmetic-sum-based decoding is significantly higher than the modulo-4 one as the probability vectors being processed in the former has 7 states, while in the latter they

have only 4 states. Moreover, the update rules of the arithmetic scheme in (63) and (64) have higher complexity than those of the modulo-4 scheme in (51) and (53). Therefore, the modulo-q sum-based channel-network decoding is generally preferred over the arithmetic when $q > 2$, in applications where receiver complexity is of concern.

VII. Conclusions

In this article, the performance of IRS-aided PNC was analyzed for one-IRS and two-IRS scenarios. It was shown that IRS greatly improves the performance of TWRC systems as it can remove the CPO between the end nodes. Detailed approximate theoretical error probability analysis was provided for the two-IRS scenario which was verified using simulations. We showed for the one-IRS scenario that only one IRS panel is sufficient to jointly align the phases of the two received signals from the two end nodes. An optimization problem was formulated to compute the optimal feasible solution that maximizes the amplitudes of the received signals at the relay to minimize the PNC detection error probability. The problem was solved using an efficient algorithm where the considered search space (feasible set) was a Riemannian manifold due to the non-convex IRS constraints. Finally, we demonstrated that using the IRS technology to enhance the PNC systems is effective in practical communication systems where channel coding and higher-order modulations are mandatory. Using IRS, we were able to design a low-complexity channel-coded PNC with any modulation order without any significant performance degradation as in conventional PNC scenarios.

References

[1] P. Chen, Z. Xie, Y. Fang, Z. Chen, S. Mumtaz, and J. J. P. C. Rodrigues, "Physical-layer network coding: An efficient technique for wireless communications," *IEEE Netw.*, vol. 34, no. 2, pp. 270–276, 2020.

[2] H. Pan, L. Lu, and S. C. Liew, "Practical power-balanced non-orthogonal multiple access," *IEEE J. Sel. Areas Commun.*, vol. 35, no. 10, pp. 2312–2327, 2017.

[3] Z. Sun, L. Yang, J. Yuan, and D. W. K. Ng, "Physical-layer network coding based decoding scheme for random access," *IEEE Trans. Veh. Technol.*, vol. 68, no. 4, 2019.

[4] A. Naeem, M. H. Rehmani, Y. Saleem, I. Rashid, and N. Crespi, "Network coding in cognitive radio networks: A comprehensive survey," *IEEE Commun. Surv. Tutor.*, vol. 19, no. 3, pp. 1945–1973, 2017.

[5] M. A. ElMossallamy, H. Zhang, L. Song, K. G. Seddik, Z. Han, and G. Y. Li, "Reconfigurable intelligent surfaces for wireless communications: Principles, challenges, and opportunities," *IEEE Trans. Cognitive Commun. Netw.*, vol. 6, no. 3, pp. 990–1002, 2020.

[6] E. Basar, M. Di Renzo, J. De Rosny, M. Debbah, M.-S. Alouini, and R. Zhang, "Wireless communications through reconfigurable intelligent surfaces," *IEEE Access*, vol. 7, pp. 116 753–116 773, 2019.

[7] M. Di Renzo, M. Debbah, D.-T. Phan-Huy, A. Zappone, M.-S. Alouini, C. Yuen, V. Sciancalepore, G. C. Alexandropoulos, J. Hoydis, H. Gacanin, J. de Rosny, A. Bounceur, G. Lerosey, and M. Fink, "Smart radio environments empowered by reconfigurable ai meta-surfaces: an idea whose time has come," *EURASIP J. Wireless Commun. Netw.*, 2019.

[8] Y.-C. Liang, R. Long, Q. Zhang, J. Chen, H. V. Cheng, and H. Guo, "Large intelligent surface/antennas (lisa): Making reflective radios smart," *J. Commun. Inform. Netw.*, vol. 4, no. 2, pp. 40–50, 2019.

[9] Q. Wu, S. Zhang, B. Zheng, C. You, and R. Zhang, "Intelligent reflecting surface-aided wireless communications: A tutorial," *IEEE Trans. Commun.*, vol. 69, no. 5, pp. 3313–3351, 2021.

[10] Q. Wu and R. Zhang, "Intelligent reflecting surface enhanced wireless network via joint active and passive beamforming," *IEEE Trans. Wireless Commun.*, vol. 18, no. 11, pp. 5394–5409, 2019.

[11] C. Huang, A. Zappone, G. C. Alexandropoulos, M. Debbah, and C. Yuen, "Reconfigurable intelligent surfaces for energy efficiency in wireless communication," *IEEE Trans. Wireless Commun.*, vol. 18, no. 8, pp. 4157–4170, 2019.

[12] C. Huang, R. Mo, and C. Yuen, "Reconfigurable intelligent surface assisted multiuser miso systems exploiting deep reinforcement learning," *IEEE J. Sel. Areas Commun.*, vol. 38, no. 8, pp. 1839–1850, 2020.

[13] M. A. ElMossallamy, H. Zhang, R. Sultan, K. G. Seddik, L. Song, G. Y. Li, and Z. Han, "On spatial multiplexing using reconfigurable intelligent surfaces," *IEEE Wireless Commun. Lett.*, vol. 10, no. 2, pp. 226–230, 2021.

[14] M. Zeng, X. Li, G. Li, W. Hao, and O. A. Dobre, "Sum rate maximization for irs-assisted uplink noma," *IEEE Commun. Lett.*, vol. 25, no. 1, pp. 234–238, 2021.

[15] X. Mu, Y. Liu, L. Guo, J. Lin, and N. Al-Dhahir, "Exploiting intelligent reflecting surfaces in noma networks: Joint beamforming optimization," *IEEE Trans. Wireless Commun.*, vol. 19, no. 10, pp. 6884–6898, 2020.

[16] G. Yang, X. Xu, and Y.-C. Liang, "Intelligent reflecting surface assisted non-orthogonal multiple access," in *2020 IEEE Wireless Commun. Netw. Conf. (WCNC)*, 2020, pp. 1–6.

[17] C. Pan, H. Ren, K. Wang, M. Elkashlan, A. Nallanathan, J. Wang, and L. Hanzo, "Intelligent reflecting surface aided mimo broadcasting for simultaneous wireless information and power transfer," *IEEE J. Sel. Areas Commun.*, vol. 38, no. 8, pp. 1719–1734, 2020.

[18] Q. Wu, X. Guan, and R. Zhang, "Intelligent reflecting surface-aided wireless energy and information transmission: An overview," *Proceedings of the IEEE*, vol. 110, no. 1, pp. 150–170, 2022.

[19] M. Al-Jarrah, E. Alsusa, A. Al-Dweik, and D. K. C. So, "Capacity analysis of irs-based uav communications with imperfect phase compensation," *IEEE Wireless Commun. Lett.*, vol. 10, no. 7, pp. 1479–1483, 2021.

[20] X. Zhou, S. Yan, Q. Wu, F. Shu, and D. W. K. Ng, "Intelligent reflecting surface (irs)-aided covert wireless communications with delay constraint," *IEEE Trans. Wireless Commun.*, vol. 21, no. 1, pp. 532–547, 2022.

[21] C. Pan, H. Ren, K. Wang, J. F. Kolb, M. Elkashlan,

M. Chen, M. Di Renzo, Y. Hao, J. Wang, A. L. Swindlehurst, X. You, and L. Hanzo, "Reconfigurable intelligent surfaces for 6g systems: Principles, applications, and research directions," *IEEE Commun. Mag.*, vol. 59, no. 6, pp. 14–20, 2021.

[22] L. Lu and S. C. Liew, "Asynchronous physical-layer network coding," *IEEE Trans. Wireless Commun.*, vol. 11, no. 2, pp. 819–831, 2012.

[23] L. Yang, T. Yang, J. Yuan, and J. An, "Achieving the near-capacity of two-way relay channels with modulation-coded physical-layer network coding," *IEEE Trans. Wireless Commun.*, vol. 14, no. 9, 2015.

[24] H. Zhang, L. Zheng, and L. Cai, "Design and analysis of heterogeneous physical layer network coding," *IEEE Trans. Wireless Commun.*, vol. 15, no. 4, 2016.

[25] S. Shukla, V. T. Muralidharan, and B. S. Rajan, "Wireless network-coded accumulate–compute-and-forward two-way relaying," *IEEE Trans. Veh. Technol.*, vol. 65, no. 3, pp. 1367–1381, 2016.

[26] L. Guo, Z. Ning, Q. Song, Y. Cui, and Z. Chen, "Toward efficient 5G transmission: SER performance analysis for asynchronous physical-layer network coding," *IEEE Access*, vol. 4, pp. 5083–5097, 2016.

[27] P. Chen, S. C. Liew, and L. Shi, "Bandwidth-efficient coded modulation schemes for physical-layer network coding with high-order modulations," *IEEE Trans. Commun.*, vol. 65, no. 1, pp. 147–160, 2017.

[28] A. Schmidt, R. Schober, and W. H. Gerstacker, "Nonlinear equalization approaches for physical layer network coding," *IEEE Trans. Wireless Commun.*, vol. 16, no. 2, pp. 825–838, 2017.

[29] H. Zhang and L. Cai, "Design of channel coded heterogeneous modulation physical layer network coding," *IEEE Trans. Veh. Technol.*, vol. 67, no. 3, 2018.

[30] T. Peng, Y. Wang, A. G. Burr, and M. R. Shikh-Bahaei, "Physical layer network coding in network mimo: A new design for 5g and beyond," *IEEE Trans. Commun.*, vol. 67, no. 3, pp. 2024–2035, 2019.

[31] Z. Wang and S. C. Liew, "Coherent detection for short-packet physical-layer network coding with binary fsk modulation," *IEEE Trans. Wireless Commun.*, vol. 19, no. 1, pp. 279–292, 2020.

[32] Y. Shao, S. C. Liew, and L. Lu, "Asynchronous physical-layer network coding: Symbol misalignment estimation and its effect on decoding," *IEEE Trans. Wireless Commun.*, vol. 16, no. 10, pp. 6881–6894, 2017.

[33] T. Koike-Akino, P. Popovski, and V. Tarokh, "Denoising maps and constellations for wireless network coding in two-way relaying systems," in *IEEE Global Telecommun. Conf.*, 2008, pp. 1–5.

[34] S. Liu, Z. Gao, J. Zhang, M. D. Renzo, and M.-S. Alouini, "Deep denoising neural network assisted compressive channel estimation for mmwave intelligent reflecting surfaces," *IEEE Trans. Veh. Technol.*, vol. 69, no. 8, pp. 9223–9228, 2020.

[35] A. Taha, Y. Zhang, F. B. Mismar, and A. Alkhateeb, "Deep reinforcement learning for intelligent reflecting surfaces: Towards standalone operation," in *2020 IEEE 21st Int. Workshop Signal Process. Advances Wireless Commun. (SPAWC)*, 2020, pp. 1–5.

[36] C. Liu, X. Liu, D. W. K. Ng, and J. Yuan, "Deep residual learning for channel estimation in intelligent reflecting surface-assisted multi-user communications," *IEEE Trans. Wireless Commun.*, vol. 21, no. 2, pp. 898–912, 2022.

[37] A. H. A. Bafghi, V. Jamali, M. Nasiri-Kenari, and R. Schober, "Degrees of freedom of the k-user interference channel in the presence of intelligent reflecting surfaces," 2021.

[38] A. Papoulis and U. Pillai, *Probability, random variables and stochastic processes*, 4th ed. McGraw-Hill, Nov. 2001.

[39] S. Nadarajah and S. Kotz, "Exact distribution of the max/min of two gaussian random variables," *IEEE Trans. Very Large Scale Integr. VLSI Syst.*, vol. 16, no. 2, pp. 210–212, 2008.

[40] C. Pan, H. Ren, K. Wang, W. Xu, M. Elkashlan, A. Nallanathan, and L. Hanzo, "Multicell MIMO communications relying on intelligent reflecting surfaces," *IEEE Trans. Wireless Commun.*, vol. 19, no. 8, 2020.

[41] X. Yu, D. Xu, and R. Schober, "MISO wireless communication systems via intelligent reflecting surfaces : (invited paper)," in *2019 IEEE/CIC Int. Conf. Commun. in China (ICCC)*, 2019, pp. 735–740.

[42] M. A. ElMossallamy, K. G. Seddik, W. Chen, L. Wang, G. Y. Li, and Z. Han, "RIS optimization on the complex circle manifold for interference mitigation in interference channels," *IEEE Trans. Veh. Technol.*, vol. 70, no. 6, pp. 6184–6189, 2021.

[43] P.-A. Absil, R. Mahony, and R. Sepulchre, *Optimization Algorithms on Matrix Manifolds*. Princeton, NJ: Princeton University Press, 2008.

[44] M. C. Pinar and S. A. Zenios, "On smoothing exact penalty functions for convex constrained optimization," *SIAM J. Optimization*, vol. 4, no. 3, 1994.

[45] C. Liu and N. Boumal, "Simple algorithms for optimization on riemannian manifolds with constraints," *Appl Math Optim*, vol. 82, no. 3, pp. 949–981, 2020.

[46] N. Boumal, B. Mishra, P.-A. Absil, and R. Sepulchre, "Manopt, a MATLAB toolbox for optimization on manifolds," *J. Machine Learning Research*, vol. 15, no. 42, pp. 1455–1459, 2014. [Online]. Available: https://www.manopt.org

[47] S. Zhang and S.-C. Liew, "Channel coding and decoding in a relay system operated with physical-layer network coding," *IEEE J. Sel. Areas Commun.*, vol. 27, no. 5, pp. 788–796, 2009.

Mahmoud AlaaEldin (M'21) received his B.Sc. in Electrical Engineering from Alexandria University, Alexandria, Egypt, in 2013. He received the M.Sc. from the American University in Cairo (AUC), Cairo, Egypt, in 2019. He is currently a Ph.D. student and a researcher at Electrical and Electronic Engineering department, The University of Manchester, Manchester, UK. Through his years at AUC, Mahmoud was a graduate fellow and a teacher assistant at the Electronics and Communications department. He received a University Fellowship from AUC in 2017 and 2018. In 2019, he received a research fellowship at the University of Manchester under the Marie Sklodowska-Curie Actions grant scheme, which is funded by the European Union's Horizon 2020 research and innovation program. His research interests include wireless communications, signal processing, multiuser MIMO/OFDM systems, massive MIMO systems, channel estimation and feedback, physical layer network coding, intelligent reflecting surfaces, optimization, and applications of machine learning in wireless communications.

Karim G. Seddik (M'04–SM'14) received the B.Sc. with an honor and M.Sc. degrees in electrical engineering from Alexandria University, Alexandria, Egypt, in 2001 and 2004, respectively, and the Ph.D. degree from the University of Maryland, College Park, MD, USA, in 2008. He is currently a Professor in the electronics and communications engineering department, at the American University in Cairo (AUC) and the Associate Dean for Graduate Studies and Research, School of Sciences and Engineering (SSE) at the AUC. Before joining AUC, he was an assistant professor at Alexandria University. His research interests include applications of machine learning in communication networks, intelligent reflecting surfaces, age of information, cognitive radio communications, and layered channel coding. Seddik has served on the technical program committees of numerous IEEE conferences in the areas of wireless networks and mobile computing.

He is the recipient of the American University in Cairo Faculty Merit Award for Excellence in Research and Creative Endeavors in 2021. He is a recipient of the State Encouragement Award in 2016 and the State Medal of Excellence in 2017. He is a recipient of the certificate of honor from the Egyptian President for being ranked first among all departments in the College of Engineering, Alexandria University in 2002. He received the Graduate School Fellowship from the University of Maryland in 2004 and 2005, and the Future Faculty Program Fellowship from the University of Maryland in 2007. He also co-authored a conference paper that received the best conference paper award from the IEEE communication society technical committee on green communications and computing in 2019.

Emad Alsusa (M'06–SM'07) completed a Ph.D. in Telecommunications from the University of Bath in the United Kingdom in 2000 and in the same year he was appointed to work on developing high data rates systems as part of an industrial project based at Edinburgh University. He joined Manchester University (then UMIST) in September 2003 as a faculty member where his current rank is a Reader in the Communication Engineering Group. His research interests lie in the area of Communication Systems with a focus on Physical, MAC and Network Layers including developing techniques and algorithms for array signal detection, channel estimation and equalization, adaptive signal precoding, interference avoidance through novel radio resource management techniques, cognitive radio and energy and spectrum optimization techniques. Applications of his research include cellular networks, IoT, Industry 4.0, and Powerline Communications. Emad's research work has resulted in over 200 journals and refereed conference publications mainly in top IEEE transactions and conferences. Emad has supervised over 30 PhDs to successful completion. Emad is an Editor of the IEEE Wireless communication Letters, a Fellow of the UK Higher Academy of Education, and a TPC Track Chair of a number of conferences such as VTC'16, GISN'16, PIMRC'17 and Globecom'18, as well as the General Co-Chair of the OnlineGreenCom'16 Conference. He is currently the UK representative in the International Union of Radio Science, and a Co-Chair of the IEEE Special Working Group on RF Energy Harvesting. Emad has received a number of awards including the best paper award in the international Symposium on Power Line Communications 2016 and the Wireless Communications and Networks Conference 2019.